Global Biogeochemical Cycles®

RESEARCH ARTICLE
10.1029/2025GB008503

Orbital Influences on Deep Ocean Oxygen Concentrations and Respired Carbon Storage

A. W. Jacobel[1,2], C. T. Pallone[3,4], K. M. Costa[5], R. F. Anderson[3,6], and J. F. McManus[3,6]

[1]Department of Earth and Climate Sciences, Middlebury College, Middlebury, VT, USA, [2]University of Colorado, Institute of Arctic and Alpine Research, Boulder, CO, USA, [3]Division of Geochemistry, Lamont-Doherty Earth Observatory, Palisades, NY, USA, [4]Department of Earth, Massachusetts Institute of Technology, Atmospheric and Planetary Sciences, Cambridge, MA, USA, [5]Department of Geology and Geophysics, Woods Hole Oceanographic Institution, Woods Hole, MA, USA, [6]Department of Earth and Environmental Sciences, Columbia University, Palisades, NY, USA

Abstract Quantitative records of bottom water oxygen (BWO) are critical for understanding deep ocean change through time. Because of the stoichiometric relationship between oxygen and carbon, BWO records provide insight into the physical and biogeochemical processes that control the air-sea partitioning of both gases with important implications for climate over Quaternary glacial-interglacial cycles. Here, we present new geochemical data sets from Ocean Discovery Program Site 1240 in the eastern equatorial Pacific to constrain paleoproductivity (Ba_{xs} flux) and BWO using a multiproxy approach (aU, Mn/Al, $\Delta\delta^{13}C$, and U/Ba). This combination of approaches allows us to quantitatively identify changes in BWO and to parse local and basin-wide contributions to the signal. We find that upwelling, not dust input, is responsible for driving productivity changes at the site. Changes in local carbon export are not the primary driver of changes in BWO, which instead reflect basin-wide changes driven by processes in the Southern Ocean. Our BWO results provide direct evidence for the role of orbital precession and obliquity in driving deep sea respired carbon and oxygen concentrations. We find variations in BWO on the order of ∼50 μmol/kg that occur with ∼23 kyr periodicity during the substages of Marine Isotope Stage 5, and variations of ∼100 μmol/kg on glacial-interglacial timescales. These findings have important implications for the role of insolation in driving deep ocean respired oxygen and carbon concentrations, and point to physical and biogeochemical changes in the Southern Ocean as key drivers of planetary-scale carbon change.

Key Points:

- Normalizing to ^{230}Th is critical for accurate data interpretation due to cyclic carbonate dissolution
- Obliquity and precessional-scale variability in bottom water oxygen concentrations is observed over the last 160 ka
- The bottom water oxygen signal reflects distal changes in the Southern Ocean, not local productivity

Supporting Information:

Supporting Information may be found in the online version of this article.

Correspondence to:

A. W. Jacobel,
ajacobel@middlebury.edu

Citation:

Jacobel, A. W., Pallone, C. T., Costa, K. M., Anderson, R. F., & McManus, J. F. (2025). Orbital influences on deep ocean oxygen concentrations and respired carbon storage. *Global Biogeochemical Cycles*, *39*, e2025GB008503. https://doi.org/10.1029/2025GB008503

Received 5 FEB 2025
Accepted 20 MAY 2025

Author Contributions:

Conceptualization: A. W. Jacobel, R. F. Anderson, J. F. McManus
Data curation: A. W. Jacobel, C. T. Pallone
Funding acquisition: A. W. Jacobel, K. M. Costa, J. F. McManus
Investigation: A. W. Jacobel
Methodology: K. M. Costa, R. F. Anderson
Project administration: A. W. Jacobel
Resources: A. W. Jacobel, J. F. McManus
Visualization: A. W. Jacobel
Writing – original draft: A. W. Jacobel
Writing – review & editing: A. W. Jacobel, C. T. Pallone, K. M. Costa, R. F. Anderson, J. F. McManus

1. Introduction

Bottom water oxygen (BWO) availability is a key oceanographic parameter with important implications for species' ecological ranges, abundances, and Earth's climate history. Changes in the spatial and temporal distribution of BWO may alter benthic respiration rates with fundamental implications for the distribution of carbon between active and inactive (fossil) carbon pools (Canfield, 1994). BWO availability is also an important paleoceanographic variable because of the stoichiometric relationship between the metabolic consumption of oxygen and the release of respired carbon, meaning that reconstructions of BWO concentrations can provide important bounds on deep ocean carbon storage through time (e.g., Anderson et al., 2019; Boyle, 1990; Hoogakker et al., 2015; Jaccard et al., 2009, 2016; Jacobel et al., 2017a, 2020). Quantitative constraints on BWO thus help to constrain the distribution of carbon between the atmosphere, biosphere, and deep ocean, and can ultimately help determine the key processes and feedbacks that are important for geologic carbon storage with consequential implications for global climate (see review and references in Jacobel et al., 2020 for greater detail).

We focus this study of bottom water oxygen on ODP Site 1240, in the Easternmost Equatorial Pacific (hereafter the EEEP, after Costa et al., 2017) for two reasons. First, the site is characterized by sedimentation rates that are relatively high for an open ocean site, particularly in the Pacific, on average ∼11 cm/kyr over the interval studied in this paper (Rippert et al., 2017). The high accumulation rate of the core, driven by regionally high nutrient upwelling, high surface productivity, and sediment focusing (e.g., Kienast et al., 2007; Pallone et al., 2025; Pena et al., 2008; Rafter et al., 2017; Winckler et al., 2016), allows for the reconstruction of paleoclimate records that have the potential to resolve both orbital (e.g., Jacobel et al., 2020; Pallone et al., 2025; Pena et al., 2008) and millennial-scale changes (Pallone et al., 2025). Second, while surface conditions at ODP 1240 are subject to the influence of local processes including insolation, the El Niño Southern Oscillation (ENSO) and changes in the position of the Intertropical Convergence Zone (ITCZ), both the surface and deep waters of the site originate in the Southern Ocean where their chemical compositions are set by processes that are critical for global air-sea

carbon partitioning (Sigman & Boyle, 2000; Sigman et al., 2010; Sigman & Haug, 2003). Thus, ODP 1240 is an ideal location to study records of biogeochemical processes because of the potential to draw inferences about both regional and global processes across a range of timescales.

Our particular focus in this paper is the role of obliquity and precession in driving surface productivity, deep ocean carbon storage, and BWO concentrations. Obliquity, or the angle of Earth's inclination with respect to the ecliptic plane, alters the intensity of the seasons in both hemispheres and thus also modulates intrahemispheric thermal gradients. Separately, the longitude of perihelion controls the timing of the seasons with respect to perihelion, Earth's closest approach to the sun. Given its low latitude, the equatorial Pacific might not be expected to have a prominent seasonal cycle, and, consequently, a strong response to obliquity or precession, but models have simulated changes in the equatorial Pacific's seasonal cycle due to changing precession (Clement et al., 2004; Erb et al., 2015; Timmermann et al., 2015) with implications for ENSO (Clement et al., 1999; Khon et al., 2018; Zhang et al., 2021) and Intertropical Convergence Zone characteristics (Bischoff et al., 2017; Jalihal et al., 2019; Zhang et al., 2020).

One mechanism by which the surface ocean of the equatorial Pacific may respond to precession is the "dynamical thermostat" (Clement et al., 1999) and can be illustrated as follows. At present, equatorial Pacific sea surface temperatures are warmest during March because local insolation is strong (perihelion in January) and the ITCZ is close to its southernmost position (boreal winter), which weakens the cross-equatorial wind stress and reduces upwelling, especially in the eastern equatorial Pacific where the latitudinal range of the ITCZ is more seasonally variable. This configuration results in a zonally retracted equatorial Pacific cold tongue and flattened thermocline, conditions often associated with El Niño events. In contrast, when perihelion occurs in boreal summer and local insolation is relatively strong at the same time that the ITCZ is near its northernmost position, strong cross-equatorial winds can cause a strengthening of upwelling and an intensification of the EEP cold tongue. The impact of this insolation forcing has been shown to be strongest when it occurs during boreal summer (June) (Clement et al., 1999). Indeed, numerous paleoceanographic proxies for surface ocean characteristics from across the equatorial Pacific have been interpreted as showing a pattern consistent with precession (Beaufort et al., 2001; Costa et al., 2017; Ivanova et al., 2012; Jin et al., 2024; Koutavas et al., 2002; Koutavas & Joanides, 2012; Pena et al., 2008; Rafter & Charles, 2012; Zhang et al., 2021). Here we evaluate the spectral signals in our new high-resolution data and use our findings to provide insights into the drivers of productivity in the easternmost equatorial Pacific, and to help understand whether or not surface-ocean processes influence our BWO records.

Orbital precession also has an impact on the Southern Ocean (SO) because when austral summer occurs closer to the perihelion, there is an intensification of the pole-to-equator temperature gradient at the height of the tropopause (200 hPa) that causes the speed of the Southern Hemisphere Westerly Winds (SWW) to increase when they are at their southernmost position (Persch et al., 2023). The SWW intensification causes additional wind stress at the surface of the SO, which increases upwelling (Persch et al., 2023). The seasonal shift in SWW experienced during austral summer is greater than the weakening in the austral winter, resulting in the net annual shift in air-sea CO_2 flux (Persch et al., 2023). Here, it is worth noting that in the SO, the influence of precession is opposite to that experienced by the equatorial Pacific. When the precession index is high (perihelion during austral summer) theory predicts reduced upwelling in the equatorial Pacific (Clement et al., 1999, 2000; Pena et al., 2008) and enhanced upwelling in the Southern Ocean.

In addition to precession, the SWW also respond to changes in Earth's obliquity. Specifically, when obliquity is low, extratropical thermal gradients are enhanced, the SWW strengthen and shifts southwards and SO upwelling is enhanced (Ai et al., 2020; Lu et al., 2010; Timmermann et al., 2014). Changes in the SWW (due to obliquity and/or precession) are important both for the upwelling of CO_2-rich deep waters (e.g., Ai et al., 2020; Anderson et al., 2009) and also have an influence on the formation of Antarctic Bottom Water (AABW), which in turn influences the bottom water respired carbon and oxygen signals observed at ODP 1240. We provide greater detail on these mechanistic linkages in Section 5.3.

In this study, we present previously unpublished records of sedimentary Al and Mn, as well as new data to enhance previously published low-resolution records of Ba_{xs} and U/Ba. We compare our new data with previously published records ($^{231}Pa/^{230}Th$, $\Delta\delta^{13}C$, and aU) to provide a multiproxy perspective on BWO and to identify basin-wide changes in oxygen and respired carbon concentrations. We synthesize results spanning the last two glacial cycles (~160 kyr) and use the enhanced temporal resolution of our new records (~1.5 kyr) to draw

new conclusions about the role of orbital precession and obliquity in driving deep ocean oxygen and respired carbon concentrations.

2. Proxy Systematics

2.1. Reconstructing Bottom Water Oxygen

Significant proxy development work over the last decade has sought to provide quantitative constraints on BWO concentrations using a variety of different geochemical and biological/morphological constraints (reviewed in Hoogakker et al., 2025; Jacobel et al., 2020). Because BWO conditions can reflect both upstream changes in oxygen and respired carbon, and local respiration changes, it is important to have a co-registered record of local organic carbon flux to accurately interpret the BWO records, a key conclusion of the above mentioned review articles and that is addressed in Section 2.2 below. A second conclusion reached by these authors is that BWO reconstructions should use multiple proxies, so that the conclusions are less susceptible to the biases of any one individual proxy. Here we synthesize results from four different proxies for BWO including the sedimentary concentration of authigenic uranium (aU) (Jacobel et al., 2020; Mangini et al., 2001; McManus et al., 2005), sedimentary ratios of uranium to barium (U/Ba) (Costa et al., 2023), sedimentary Mn/Al ratios (e.g., Berger et al., 1983; Mangini et al., 2001; Pavia et al., 2021), and the carbon isotope gradient ($\Delta\delta^{13}C$) between epifaunal *Cibicidoides wuellerstorfi* and infaunal *Globobulimina spp.* (Hoogakker et al., 2015; Jacobel et al., 2020; McCorkle & Emerson, 1988). The geochemical underpinnings of these proxies have been discussed in depth in the literature, so here we briefly highlight the key principles and emphasize similarities and differences among the four proxies.

2.1.1. Authigenic Uranium (aU)

The sedimentary concentration of aU, precipitated authigenically in situ, is the result of redox-driven changes in the solubility of seawater uranium. In oxic seawater U(VI) is soluble and will remain dissolved (Endrizzi & Rao, 2014). Changes in the redox state of sediments due to changes in local organic carbon flux or BWO can create reducing conditions that drive U(IV) to precipitate from porewaters, creating a concentration gradient that drives a diffusive flux into the porewaters, creating sediments high in authigenic U. This is the primary mechanism of U removal from the global oceans (Klinkhammer & Palmer, 1991; McManus et al., 2005). High sedimentary concentrations of aU are thus indicative of changes in the sedimentary redox state. The redox state of sediment depends both on the supply of organic carbon and on BWO, so it is not possible to definitively attribute aU precipitation to changes in BWO alone without a co-registered record of organic carbon flux, such as opal or Ba_{xs}. Additionally, the aU record preserved in a sediment core may be imprinted with post-depositional changes in sediment redox that can cause removal or down core remobilization of U (see review in Jacobel et al., 2020). Because removal and remobilization are difficult to track, aU cannot be used as a quantitative proxy for BWO. Its magnitude of enrichment is not directly related to BWO concentrations and thus gives only a relative sense of change. We do not interpret aU as a quantitative indicator of BWO at Site ODP 1240, but we do note that postdepositional remobilization of U is unlikely to dramatically impact the timing of observed changes in BWO at the site because the accumulation rates (~11 cm/kyr) are consistently high. The aU data considered here are from previous work (Jacobel et al., 2020; Pallone et al., 2025) and are quantified relative to co-registered ^{232}Th activities using a detrital $^{238}U/^{232}Th$ activity ratio of 0.7 ± 0.2.

2.1.2. Uranium Barium Ratios (U/Ba)

One method proposed to differentiate between redox variability driven by organic carbon fluxes versus those forced by BWO changes is to normalize uranium to barium, a productivity proxy (see Section 2.2.1 below) (Costa et al., 2023). If porewater oxygen content decreases due to an increase in organic carbon fluxes, both U and Ba contents would increase, resulting in minimal change in U/Ba. In contrast, if the porewater oxygen content decreases due to a decrease in BWO, the sedimentary U content would increase while Ba would stay the same, resulting in an increase in U/Ba. Recent coretop calibration work proposed a region-specific calibration for the EEP (Costa et al., 2023), and down-core reconstructions of U/Ba from the EEP were found to share strong similarities with previously published records of BWO (Hoogakker et al., 2018; Jacobel et al., 2020) developed using the $\Delta\delta^{13}C$ proxy for BWO (see review in Hoogakker et al., 2025). While U/Ba was able to capture similar glacial-interglacial trends as $\Delta\delta^{13}C$, there are several important differences in the recommended proxy

applications. U/Ba likely does not faithfully capture the timing of climate transitions, due to the susceptibility of uranium to diagenetic remobilization, but U/Ba does appear to more accurately capture absolute oxygen concentrations relative to $\Delta\delta^{13}C$ (Costa et al., 2023).

2.1.3. Foraminiferal Carbon Isotope Gradient ($\Delta\delta^{13}C$)

The carbon isotope ($\delta^{13}C$) difference between select species of epifaunal benthic foraminifera and infaunal benthic foraminifera has been proposed as an empirical, quantitative proxy for BWO (Hoogakker et al., 2015, 2025) following earlier work to establish the theoretical basis for the proxy (e.g., McCorkle & Emerson, 1988). The $\Delta\delta^{13}C$ proxy is based on oxic respiration in sedimentary porewaters, which releases isotopically light carbon in proportion to the abundance of oxygen in bottom waters. When oxygen concentrations are high, respiration produces significant carbon isotope differentials between bottom water (as constrained by *C. wuellerstorfi*) and porewater at the oxic/anoxic boundary (as constrained by *Globobulimina spp.*). When BWO concentrations are low, porewater respiration is limited and the gradient is proportionally smaller. Recent work (Costa et al., 2023; Jacobel et al., 2020; Lu et al., 2022; Thomas et al., 2022) has shown that BWO estimates from $\Delta\delta^{13}C$ tend to be biased high, especially in high productivity environments, likely due to contributions of isotopically light carbon from anoxic metabolic pathways including nitrate- and sulfate-reduction (Bradbury et al., 2024).

2.1.4. Manganese to Aluminum Ratios (Mn/Al)

The fourth bottom water oxygen proxy considered in this study is the ratio of Mn normalized to Al. As with aU, Mn solubility varies as a function of the porewater redox state, which may be driven by BWO or carbon flux to sediments (e.g., Mangini et al., 2001). Mn(II) is soluble and is present in reducing porewaters as $Mn_{(aq)}$ (Calvert & Pedersen, 1996). Some dissolved Mn has also been found to exist as Mn(III) due to the influence of organic ligands (Madison et al., 2013). In contrast, the more oxidized form of Mn, Mn(IV), is insoluble and present in sediments as MnO_2 (Calvert & Pedersen, 1996). Mn(IV) is used in bacterial respiration as an electron acceptor after oxygen and nitrate have been consumed (Froelich et al., 1979), reducing solid MnO_2 to soluble Mn(II), which diffuses upward in pore water until it encounters oxygen. At that point, Mn(II) is oxidized and reprecipitated as MnO_2, forming a maximum in the concentration of MnO_2 at the oxic/anoxic interface. As sediment accumulates under conditions of low BWO, a peak of solid Mn is expected to accumulate and move upward following the porewater oxic/anoxic boundary. A subsequent increase in BWO will create oxygenated conditions in pore water to a depth well below the MnO_2 peak, causing the Mn peak to be preserved and buried by ongoing sedimentation. Under conditions of alternating low and high BWO, the respiration of organic matter during intervals of high BWO may be so extensive that there is insufficient organic matter remaining to produce reducing conditions and dissolve the buried MnO_2 peaks during subsequent periods of low BWO. Consequently, one may find several peaks in MnO_2 preserved within a sediment column. For example, in the central Equatorial Pacific (140°W), preserved Mn peaks are observed in sediment covering the past million years (Pavia et al., 2021).

Because Mn is also present as a component of terrigenous materials, we normalize Mn abundances to Al to account for lithogenic inputs, although the trends are virtually identical regardless of whether Al or Fe is used to normalize Mn (Figure S1 in Supporting Information S1). The contrasting redox behaviors of Mn/Al and aU make them valuable complements in constraining the timing of bottom water oxygenation, if changes in the rain rate of organic carbon can be constrained (e.g., Pavia et al., 2021) as they are in this study.

Data reflecting sedimentary aU (Jacobel et al., 2020; Pallone et al., 2025) and $\Delta\delta^{13}C$ (Jacobel et al., 2020) at ODP 1240 have been previously published, as was a lower-resolution record of U/Ba (Costa et al., 2023). Here we synthesize the existing data with new, high-resolution Ba_{xs} and Mn data from ODP 1240, and compare them with data from nearby sites (Figure 1).

2.2. Reconstructing Paleoproductivity

The composition of marine primary production, the extent to which producers consume new versus regenerated nutrients during production, and the efficiency of organic material export to sediments are key controls on the partitioning of carbon in the Earth system (e.g., Sigman & Boyle, 2000; Sigman & Hain, 2024; Sigman & Haug, 2003). A large body of work has previously demonstrated that the EEEP (Jacobel et al., 2019; Pallone et al., 2025; Rafter et al., 2017; Robinson et al., 2009), and indeed the equatorial Pacific as a whole (Costa et al., 2016; Winckler et al., 2016), did not experience the same iron-driven enhancement of the glacial biological

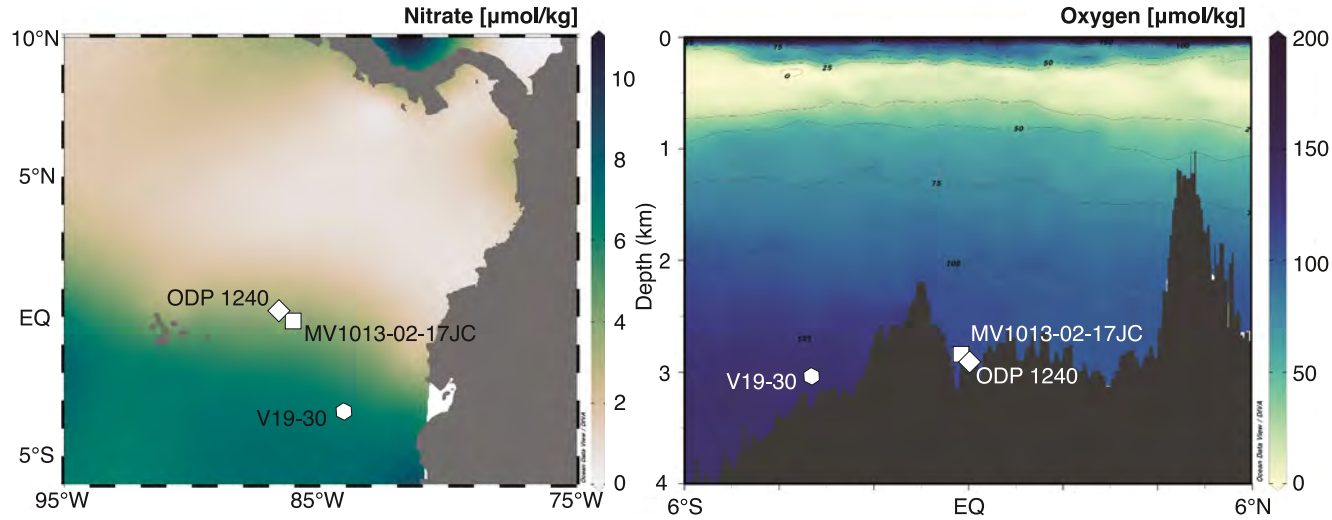

Figure 1. Map of eastern equatorial Pacific core sites. ODP Site 1240 is marked by a white diamond, MV1013-02-17JC is a white square (Loveley et al., 2017), and V19-30 (e.g., Hayes et al., 2011) is a white hexagon. Basemaps were made using the software package Ocean Data View (Schlitzer, 2016), with nitrate and oxygen data from the World Ocean Atlas (Garcia et al., 2023).

pump as did regions of the Southern Ocean (e.g., Martínez-García et al., 2014). We consider that question resolved, and here we focus instead on a record of Ba_{xs} flux to provide a local perspective on bulk organic carbon export to sediments. Previous work from the same site (Pallone et al., 2025) presented $^{231}Pa/^{230}Th$ ratios as a proxy particularly sensitive to opaline (diatom) productivity (e.g., Chase et al., 2002, 2003), and here we compare the two records and use both to inform our interpretation of multiproxy bottom water oxygen records. We expand on the basis of these proxy reconstructions in the sections that follow.

2.2.1. Non-lithogenic Barium Fluxes (Ba_{xs} Flux)

Excess barium (Ba_{xs}), or non-lithogenic Ba, has been shown to have a strong relationship with bulk organic carbon fluxes at deep, open ocean sites (Carter et al., 2020; Dymond & Collier, 1996; Dymond et al., 1992; François et al., 1995; Singh et al., 2020). Barium, in the form of barite ($BaSO_4$), is precipitated below the euphotic zone in association with the respiration of organic matter produced in the photic zone. Although the precise formation mechanism is unknown, it appears that it is precipitated in microenvironments where bacterial respiration causes supersaturation of barite and precipitation is favored (Carter et al., 2020; Hayes et al., 2021; Singh et al., 2020 and references therein). As particulate Ba sinks into the deep ocean where barite is undersaturated, a fraction of the Ba precipitated in the surface ocean dissolves, so the extent to which barite is preserved is a function of exposure to undersaturated conditions (Carter et al., 2020) and redox state (Falkner et al., 1993). Accordingly, barite preservation is a function of both basin Ba concentration and site depth (Singh et al., 2020) with lower barite preservation at sites that are more undersaturated and/or deeper. The deep Panama Basin is thus one of the best locations to use Ba as a productivity proxy because (a) dissolved Ba concentrations are among the highest in any ocean basin (least undersaturation) (Carter et al., 2020 and references therein), (b) the bottom waters remained oxic throughout the time period studied (based on the $\Delta\delta^{13}C$ reconstruction from Jacobel et al., 2020 and the abundance of benthic foraminifera *C. wuellerstorfi* throughout the core). We use our new data to make inferences about qualitative trends in organic carbon export through time but refrain from making quantitative inferences about the total amount of organic carbon exported to sediments.

2.2.2. Protactinium Thorium Ratios ($^{231}Pa/^{230}Th$)

This study compares new Ba_{xs}-derived estimates of organic carbon flux to sediments with $^{231}Pa_{xs,0}/^{230}Th_{xs,0}$ ratios (hereafter $^{231}Pa/^{230}Th$) from ODP 1240 published by Pallone et al., 2025. As with ^{230}Th, ^{231}Pa is produced by the decay of well-mixed ($\tau = 400$ kyr) uranium in the water column (Henderson & Anderson, 2003) and both daughter isotopes (^{230}Th, ^{231}Pa) are scavenged by particles descending through the water column, although Th experiences a rate of absorption that is an order of magnitude greater than that of Pa (Hayes et al., 2014; Henderson & Anderson, 2003). The $^{231}Pa/^{230}Th$ ratio in the Pacific is dependent primarily on the composition of

settling particles with secondary influences from the total particle flux to the seafloor (Henderson & Anderson, 2003). Particle composition is a critical variable to consider when interpreting the $^{231}Pa/^{230}Th$ proxy because Pa preferentially sorbs to opal, whereas Th sorbs weakly to opal and preferentially to $CaCO_3$ (Chase et al., 2002, 2003; Hayes et al., 2015; Henderson & Anderson, 2003).

In the EEEP, the influence of particle composition on sedimentary $^{231}Pa/^{230}Th$ is reinforced by the high particle fluxes driven by upwelling-induced productivity. Because of its longer residence time in the water column compared to ^{230}Th, ^{231}Pa is more susceptible to export from low particle flux regions (e.g., the central Pacific gyres) to high particle flux regions such as the EEP and EEEP (Hayes et al., 2014). Thus, a combination of particle composition and flux allows the $^{231}Pa/^{230}Th$ activity ratio of EEP sediments to be higher than that predicted by the production ratio (0.093) (Anderson et al., 1983; Chase et al., 2002). Previous work in the Line Islands region of the central equatorial Pacific (CEP) has shown that there are strong relationships between $^{231}Pa/^{230}Th$ and opal flux ($r^2 = 0.90$, $p < 0.001$), and between $^{231}Pa/^{230}Th$ and Ba_{xs} flux ($r^2 = 0.85$, $p < 0.01$) (Costa et al., 2016), consistent with observations across other equatorial Pacific regions (e.g., François et al., 1993). However, the specific relationship between Pa/Th and other productivity proxies may not scale linearly with organic carbon fluxes. First, the relationship between Ba_{xs} and C_{org} varies regionally, for example, as a function of dissolved barium concentrations, and the undersaturation of barium at the depth of preservation (see review in Carter et al., 2020). Second, the relationship between $^{231}Pa/^{230}Th$ and Ba_{xs} might be decoupled if the species assemblage of surface productivity were to shift toward diatoms (i.e., because $^{231}Pa/^{230}Th$ is more strongly influenced by opal). Finally, the relationship might be entirely decoupled if the preservation of Ba_{xs} is influenced by sulfate reduction (Carter et al., 2020), which is not thought to influence $^{231}Pa/^{230}Th$. Using our new data, we evaluated the strength of the relationship between $^{231}Pa/^{230}Th$ and Ba_{xs} in the EEEP. The $^{231}Pa/^{230}Th$ data (and ^{232}Th-based dust fluxes) from ODP 1240 have been previously published (Pallone et al., 2025).

3. Methods

3.1. Core Site

Ocean Discovery Program (ODP) Site 1240 (0.0°N, 86.5°W, 2,921 m) (Figure 1) has provided many important records of eastern equatorial Pacific paleoclimate since its recovery in 2002 (e.g., Calvo et al., 2011; de la Fuente et al., 2015; Jacobel et al., 2020; Pallone et al., 2025; Pena et al., 2008; Pichevin et al., 2009; Rippert et al., 2017). The site lies just east of the Galapagos Islands, on the northern flank of the Carnegie Ridge, within the Panama Basin. The physical oceanography of the region east of the Galapagos Islands has remained a longstanding question in the literature (Karnauskas et al., 2010; Kessler, 2006). Some authors have asserted that the eastward flowing Equatorial Undercurrent (EUC) continues east of the Galapagos Islands (Pak & Zaneveld, 1973; Stevenson & Taft, 1971), while others have suggested that the flow is disrupted or bifurcated by the Galapagos Islands (e.g., Karnauskas et al., 2010, 2020) with the southern branch intersecting the northwestward flowing Peru Current and directing EUC waters to the surface east of the Galapagos (Kessler, 2006 and references therein). Despite uncertainty as to how precisely the EUC navigates the Galapagos Islands, surface waters at the site are predominantly sourced from the EUC (summary in Kessler, 2006; Mix & Tiedmann, 2003; Pena et al., 2008). Bottom waters at ODP Site 1240 are derived from North Pacific Deep Water (NPDW) with flow moving northward from the Peru Basin and entering the Panama Basin through a gap in the Carnegie Ridge (Fiedler & Talley, 2006). The waters that bathe our site actually originate as Antarctic Bottom Water (AABW) in the Ross Sea (Solodoch et al., 2022), and as they move northward away from the Antarctic margin, they mix to form Lower Circumpolar Deep Waters (LCDW) (Kawabe & Fujio, 2010). As these waters continue to move northward in the abyssal Pacific, they age, accumulate respired carbon, mix with intermediate waters and move upward in the water column (Kawabe & Fujio, 2010). These waters are "renamed" NPDW as they reach their northernmost extent in the North Pacific (20–30°N) and begin their return flow southward as NPDW, which ultimately reaches the Antarctic Circumpolar Current (Kawabe & Fujio, 2010).

Site 1240 has experienced continuous deposition over the last ~160 ka with sedimentation rates averaging ~11 cm/kyr (Rippert et al., 2017). The age model for the site (Pallone et al., 2025; Pena et al., 2008; Rippert et al., 2017) was determined using both ^{14}C dates (for the first 5.2 mcd) and benthic foraminifera $\delta^{18}O$ alignment with the LR04 stack (Lisiecki & Raymo, 2005). The site has experienced significant sediment focusing with ^{230}Th-based focusing factors in the range of 4–7 over the last 160 ka (Pallone et al., 2025), consistent with previous work showing high focusing factors in this region (François et al., 2007; Kienast et al., 2007; Singh

et al., 2011). Sedimentation rates and focusing factors are consistently high over the study interval, suggesting that changes in sedimentary redox state as tracked by aU and Mn/Al are unlikely to be driven by these variables (see review in Hoogakker et al., 2025). In this study, we compare records from ODP Site 1240 to nearby core sites MV1013-02-17JC (hereafter 17JC) (0.2°S, 85.9°W, 2,846 m), which sits just 70 km to the SE of our study site, and V19-30 (3.4°S, 83.5°W, 3,091 m) (Figure 1).

3.2. Major Element Geochemistry

The major elemental composition of ODP Site 1240 sediments was determined via ICP-OES at the Lamont-Doherty Earth Observatory of Columbia University. For each sample ∼50 mg of bulk sediment was digested at 300°C using HNO_3, HF, and $HClO_4$. Samples were diluted using 0.5N HNO_3 and were analyzed alongside synthetic calibration standards to constrain instrument response over the range of sample concentrations. Samples were run with an internal standard, and 26 replicates were run between two batches to ensure reproducibility. This analytical approach is identical to that used for samples previously published on the site (Jacobel et al., 2019). The relative standard deviation of the internal standards (the Line Islands Mega Standard—"LIMS", and the VOICE Mega Standard—"VIMS"), separately digested and analyzed ($n = 7$), averaged 3.1% for Ba, 1.1% for Fe, 1.6% for Al, and 6.1% for Mn. The average standard deviation of 26 replicates (two or more separately digested and analyzed samples) was 0.10 mg/g or ∼4.2% of average sample values for Ba, 0.33 mg/g or 3.2% of average sample values for Fe, 0.78 mg/g or 5.5% of average sample values for Al, and 0.21 mg/g or 8.3% of average sample values for Mn. We report these standard deviations as the one sigma uncertainty of measurements for each element.

Non-lithogenic Ba (Ba_{xs}) was quantified using a Ba/Al terrigenous ratio of 0.0075 (Dymond et al., 1992; François et al., 1995; Hans Wedepohl, 1995). Within the range of locally measured and predicted terrigenous Ba/Al ratios for the Pacific (0.0051–0.0075) (see review in Reitz et al., 2004), the maximum difference in Ba_{xs} concentrations is 0.05 mg/g, or on average about 1.5% of reconstructed Ba_{xs} concentrations. We therefore conclude that neither our absolute reconstructed values, nor the down core trends are sensitive to the choice of terrigenous ratio. Corrections for the terrigenous fraction were determined to be less than 10% of the measured Ba, as illustrated by the similarity between Figure 2 panels D and E. Previous work at 17JC has established that in this region there is no difference between Ba_{xs} fluxes that are calculated using Ba/Al terrigenous ratios and the $Ba/^{232}Th$ terrigenous ratios (Singh et al., 2020). Ba_{xs}, Fe, and Al concentrations were flux-normalized using previously published ^{230}Th data (Jacobel et al., 2020; Pallone et al., 2025) following standard methods (Costa et al., 2020). Mn concentration data are reported relative to Al concentrations to account for lithogenic inputs. These data have not been flux normalized as they represent in situ authigenic precipitation (Pavia et al., 2021). As previously noted, trends in Mn/Al are virtually the same as those in Mn/Fe, as illustrated in Figure S1 of Supporting Information S1.

4. Results

4.1. Major Element Concentration Results

New data double the previously available resolution of the major element concentration data from Site ODP 1240 (Jacobel et al., 2025). Concentration data appear to vary smoothly with a high signal-to-noise ratio (Figure 2). Aluminum concentrations decrease from Marine Isotope Stage (MIS) 6 into Termination II (TII), and then increase through MIS5 to their highest values before declining into MIS2/3/4. Manganese concentrations display overall low values (∼1–3 mg/g) and muted variability with the exception of peaks (5–16 mg/g) centered at ∼130, 117, 95, 73, 48 and 9 ka. Iron concentrations share significant variability with the Al data, but reach a maximum at 9 ka. Barium and excess barium concentrations are low during MIS6 and increase into MIS 5 and display striking 23 ka cyclicity before declining into MIS 2/3/4 levels that are comparable to MIS 6 concentrations. The gap in the data around 90 ka is due to the influence of the Los Chocoyos ash (Drexler et al., 1980), which has an anomalous geochemical signal, specifically in thorium and aluminum that is not relevant to the present study.

5. Discussion

5.1. Importance of Flux Normalization

A substantial body of work has illustrated the importance of considering flux-normalized sedimentary data (e.g., Costa et al., 2020 and references therein) because of multiple variable inputs and the significant potential for syn-

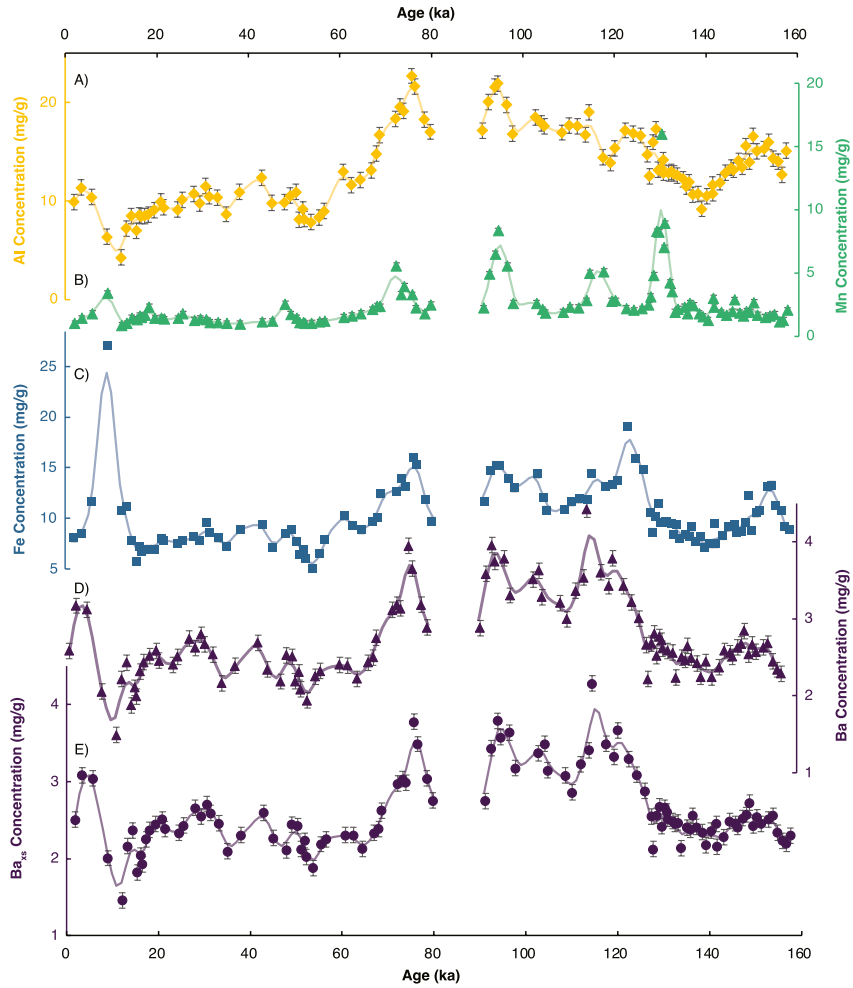

Figure 2. Major element concentrations from ODP 1240. (a) Aluminum (mg/g) gold diamonds, (b) manganese (mg/g) green triangles, (c) iron (mg/g) blue squares, (d) barium (mg/g) purple triangles and (e) excess barium (mg/g) purple circles. All data are displayed with one sigma uncertainty estimates although in some cases these are smaller than the symbols themselves. Solid lines show the 5 kyr bandpass filter of data. The gap just before 80 ka represents data that were influenced by an ash layer (exceptionally high concentrations) and are not interpreted in this study.

and post-depositional processes to influence the preserved sedimentary record. The relevance of one of these processes, sediment focusing, has been previously emphasized for the Panama Basin (Kienast et al., 2007) and here we provide new evidence that carbonate dissolution also plays a significant role in the post-depositional modification of the region's sedimentary composition. We focus our interpretation on data younger than ∼130 ka because of the larger uncertainties associated with ^{230}Th fluxes beyond that time period (Note S1 in Supporting Information S1).

Our data show that the record of Ba_{xs} concentration from ODP 1240 (Figure 3a) is strikingly different from the flux-normalized record (Figure 3c) (^{230}Th-based fluxes from Jacobel et al., 2020; Pallone et al., 2025), suggesting that sedimentary concentrations have been heavily modified by a process acting at or near the seafloor. Specifically, while concentration data are suggestive of interglacial Ba_{xs} export that is significantly higher than glacial levels, the ^{230}Th-normalized data reveal that glacial fluxes of Ba_{xs} are actually comparable to interglacial fluxes (2–3 mg/cm^2/ka). The latter conclusion is consistent with a large and growing body of research that has demonstrated similar or lower glacial productivity relative to interglacial periods across the equatorial Pacific (Bradtmiller et al., 2010; Costa et al., 2016, 2017a; Hayes et al., 2011; Kienast et al., 2006; Winckler et al., 2016). Not only do the concentration data give an inaccurate sense of the relative glacial versus interglacial export

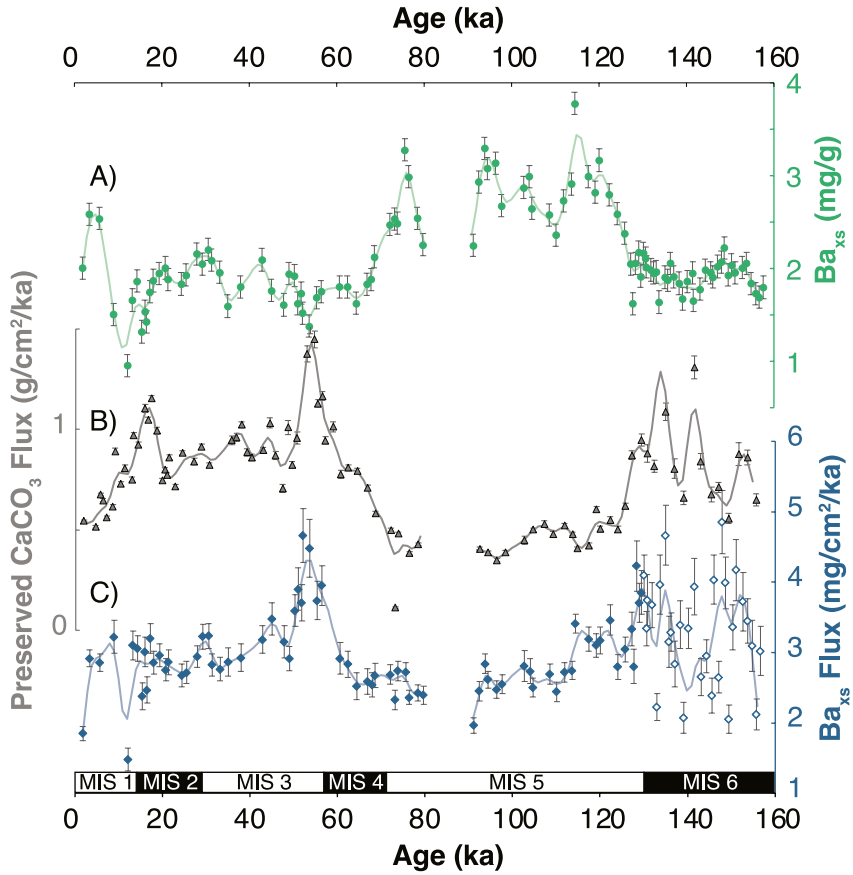

Figure 3. Eastern equatorial Pacific geochemical data. (a) Ba_{xs} concentrations (mg/g) (green circles), (b) preserved carbonate flux (g/cm^2/ka) (gray triangles) (Pallone et al., 2025), and (d) Ba_{xs} flux (mg/cm^2/ka) (blue diamonds). All geochemical data are displayed with one sigma uncertainty estimates. Solid lines show the 5 kyr bandpass filtered data. The gap just before 80 ka in some data sets represents data that were influenced by an ash layer (exceptionally high concentrations and fluxes) and are not interpreted in this study. Open symbols in c represent flux-normalized data older than 130 ka which have large uncertainties (Note S1 in Supporting Information S1).

production, the strong ~21 ka cyclicity apparent in the Ba_{xs} concentration data during MIS 5 is dramatically diminished in the flux-normalized data (Figures 3a and 3c).

We argue that the stark differences between the pattern of major element concentration data versus the flux-normalized at ODP 1240 are strongly suggestive of calcium carbonate dissolution. Unambiguous differences in concentration data relative to flux normalized data have previously been shown to occur as a consequence of carbonate dissolution on glacial-interglacial timescales (e.g., Skonieczny et al., 2019). It is evident that during time periods when $CaCO_3$ preservation is low (Figure 3b), the major element concentrations are elevated. We suggest that the concentration of major elements is primarily driven by calcium carbonate dissolution. Thus, only when flux-normalized does Ba_{xs} reflect changes in the export of organic matter from the surface of the ocean to the seafloor. Here, we present two lines of evidence to support our interpretation of carbonate dissolution changes as driving differences between our concentration and flux-normalized records.

First, Ba, Al, Fe, and Mn have shared variability in their concentration patterns (Figure 2) despite a diversity of production/source functions. This common signal is most easily explained by variable post-depositional $CaCO_3$ dissolution; because concentrations are relative and must sum to 100%, the loss of one sedimentary component ($CaCO_3$) requires that the concentrations of all the others (e.g., Al, Ba) increase. Second, at open ocean sites in the eastern Equatorial Pacific, like ODP 1240, marine sediments are dominated by calcium carbonate. *Preserved* carbonate mass flux data from ODP 1240 show an antiphase relationship with the Ba concentration data (Figure 3 panels A and B) and suggest that changes in the preservation of $CaCO_3$ can substantially influence the relative

concentrations of the other sedimentary constituents. This interpretation is consistent with previous work from the central equatorial Pacific that interpreted $CaCO_3$ fluxes as primarily reflective of preservation rather than production and suggested post-depositional modification of preserved $CaCO_3$ fluxes by corrosive bottom waters (Anderson et al., 2008). Here, the appearance of precessional-scale variability in the major element concentrations at Site 1240 is enhanced by variations in the preservation of $CaCO_3$ forced by upstream changes in respired carbon storage (e.g., Jaccard et al., 2009; Jacobel et al., 2020) and alkalinity (Rickaby et al., 2010). Indeed, precessionally forced changes in Panama and Peru Basin carbonate preservation have been previously documented (Ivanova et al., 2012; Weber et al., 1995).

Given the susceptibilityof deep-sea calcium carbonate to variations in preservation, we recommend that any record seeking to evaluate orbital periodicities in sedimentary constituents be flux normalized, to avoid mistakenly interpreting a sedimentary signal as deriving solely from changes in the proxy source function (primary productivity for Ba_{xs}), when it may experience multiple influences. This is not a novel recommendation (Costa et al., 2020), but the major element concentration records at ODP Site 1240 provide a particularly dramatic example of how failure to account for primary or secondary dilution effects may lead to incorrect data interpretations.

5.2. Paleoproductivity

Constraining changes in export productivity in the equatorial Pacific is critical, both for understanding whether local changes in productivity can affect the partitioning of carbon between the ocean and atmosphere (reflecting true changes in the ocean's biological pump), and for diagnosing the mechanisms responsible for productivity changes. Our new Ba_{xs} fluxes, in combination with recently published $^{231}Pa/^{230}Th$ data also from ODP 1240 (Pallone et al., 2025) (Figure 4), provide independent perspectives on two different components of primary production: total organic flux and opaline (siliceous) flux, and help to answer important questions about carbon cycle change and precession as a driver. Here we focus on identifying the mechanisms responsible for changing productivity and in Section 5.3 we address their relevance for carbon partitioning.

5.2.1. Evaluating Changes in Paleoproductivity and Drivers

Beginning at the MIS 6–5 transition (Termination II, or TII) at ∼141 ka (Drysdale et al., 2009) Ba_{xs} fluxes show an increase in productivity (Figure 4e) that is consistent with previously published records of opal flux from the EEP and CEP (Hayes et al., 2011), suggesting that surface ocean productivity with respect to both diatoms and bulk organic material was enhanced. This increase in paleoproductivity has been tied to the supply of nutrients from the Southern Ocean (Hayes et al., 2011; Pena et al., 2008) and might have been enhanced by the decreasing index of precession that would be expected to lead to stronger EEP upwelling (Clement et al., 1999, 2000; Pena et al., 2008). These influences may have been briefly muted by a southward shift of the ITCZ (Jacobel et al., 2016; Reimi et al., 2019) that occurred during Heinrich Stadial 11 (136–129 kyr), and which would have weakened cross—equatorial winds and decreased divergence. This may explain some of the structure in the records at this time. However, increased organic export (this study), a peak in opal flux from V19-30, another EEEP site (Hayes et al., 2011), and a shallower thermocline and cooler sea surface temperatures (Pena et al., 2008) suggest that the net deglacial impact included enhanced upwelling in the EEP. The strong increase in Ba_{xs} fluxes (second in magnitude only to the peak at ∼53 ka) and opal flux (Hayes et al., 2011) over TII and decrease into MIS 5e are not entirely consistent with the $^{231}Pa/^{230}Th$ data (Figure 4f), which do not show as strong an increase, or as observed in the CEP (Hayes et al., 2011). These differences are discussed further in Section 5.2.2.

After MIS 5e ends at ∼115 ka, both Ba_{xs} fluxes and $^{231}Pa/^{230}Th$ show consistent, relatively low export to sediments during the remainder of the MIS 5 substages (a–d) (Figure 4). Both proxies show their largest increase in sedimentary export flux at ∼53 ka, a feature previously identified in opal flux and $^{231}Pa/^{230}Th$ records from the EEP (Hayes et al., 2011; Kienast et al., 2006; Pallone et al., 2025). The appearance of this export production peak, in both $^{231}Pa/^{230}Th$ and Ba_{xs} flux, supports the interpretation put forth by both Hayes et al., 2011; Kienast et al., 2006, and is supported by the low $\delta^{13}C$ of *N. dutertrei* (Pena et al., 2008; Shackleton et al., 1983), that the peak reflects an increase in productivity driven by nutrient leakage, most likely from the Southern Ocean via the Equatorial Undercurrent. The productivity increase beginning at ∼63 ka and peaking at ∼53 ka is inconsistent with the dynamical thermostat/equatorial insolation as the driver

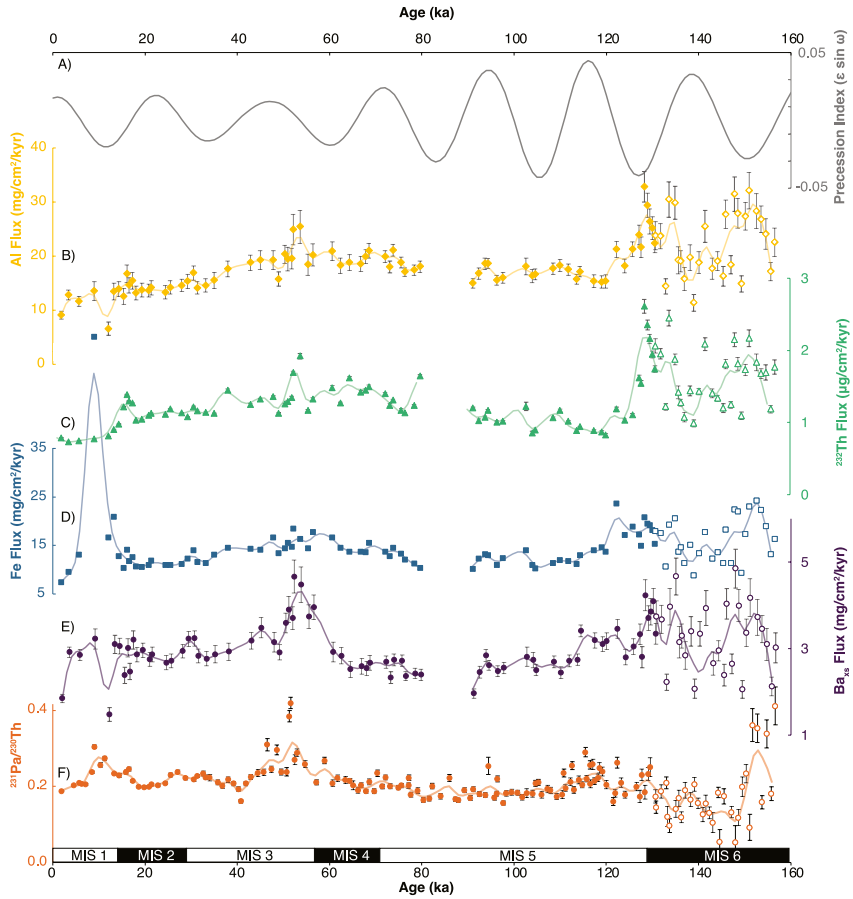

Figure 4. Elemental and isotope fluxes from ODP 1240. (a) precession index (gray line), (b) Al flux (gold diamonds and line), (c) ^{232}Th flux a proxy for aeolian dust (green triangles and line), (d) Fe flux (blue squares and line), (e) Ba_{xs} flux (purple circles and line), and (f) $^{231}Pa/^{230}Th$ from Pallone et al., 2025 (orange circles and line). All lines depict the 5 kyr lowpass filter of the data. All data are plotted with their 1σ uncertainties. Open symbols in c–f represent flux-normalized data older than 130 ka, which have large uncertainties (Note S1 in Supporting Information S1).

of the increase, as the event onset coincides with rising precession and culminates at the same time as a precession maximum (perihelion during austral summer) (Figure 4a) which should suppress upwelling in the equatorial Pacific (Clement et al., 1999; Pena et al., 2008). Therefore, it is more likely that the signal arises from high precession in driving southward shifts in the SWW during austral summer that, due to the strong asymmetry of the seasonal response, leads to an increase in the annually integrated upwelling in the SO (Persch et al., 2023) and nutrient leakage to the EEP. This hypothesis is supported by the observation that global pCO_2 levels increase during this same interval (Bereiter et al., 2015), as would be expected if increased upwelling in the SO was responsible for both the increasing nutrient and pCO_2 signals. After the export flux peak at ~53 ka, both proxies show similar export during MIS 2/3/4 as during late MIS5. Both Ba_{xs} flux and $^{231}Pa/^{230}Th$ also have some precession-scale variability during this interval, which we investigated using spectral techniques (Figure 5). Both Ba_{xs} flux and $^{231}Pa/^{230}Th$ have spectral power at 41 and 21 kyr and variability is generally in-phase, suggestive of a shared driving mechanism. The precessional power is primarily present in the proxy records over the last glacial period. At the last termination, both the Ba_{xs} flux and $^{231}Pa/^{230}Th$ records show a deglacial increase in productivity, a feature previously identified as a robust feature of equatorial Pacific flux records (Costa et al., 2017a) and attributed to changes in Southern Ocean nutrient tunneling to the equatorial Pacific and enhanced upwelling due to the local impact of precession (Pena et al., 2008).

Our finding of increased organic and siliceous productivity in the eastern equatorial Pacific, associated with changes in regional wind stress and changes in Southern Ocean upwelling and nutrient utilization, is consistent

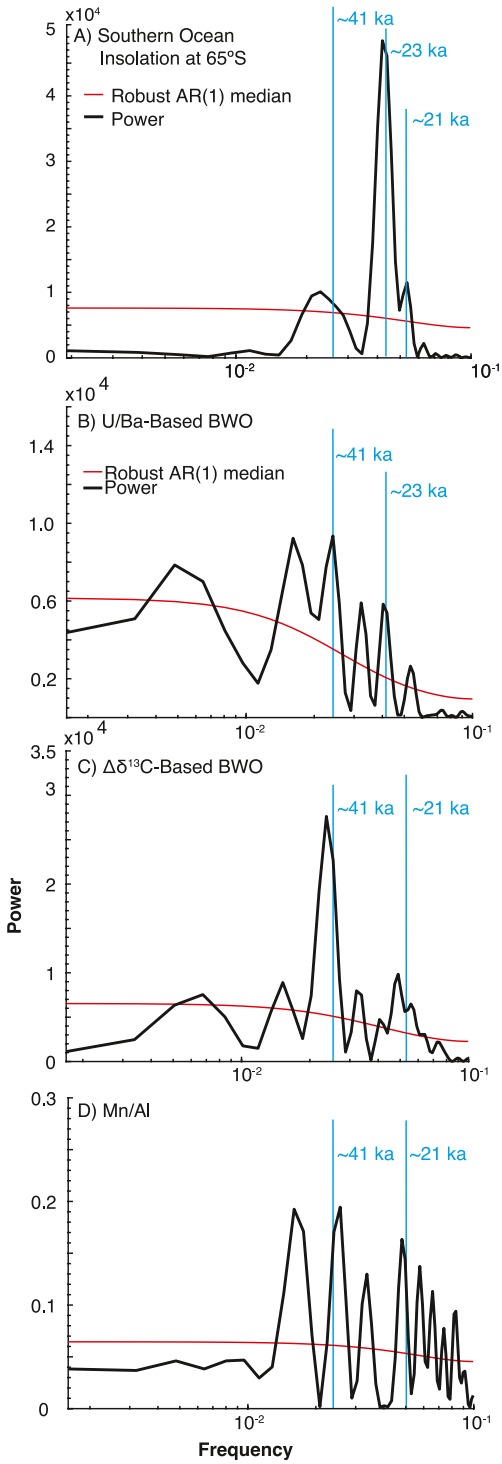

Figure 5. Spectral analysis of (a) equatorial Pacific insolation at 0°N in September, (b) Southern Ocean insolation at 65°S in January, (c) Equatorial Pacific Ba_{xs} flux, and (d) equatorial Pacific $^{231}Pa/^{230}Th$. Black lines show the power spectra of the time series, the red line is the AR(1) spectrum, and blue lines indicate peaks of power that coincide with orbital periodicities.

with existing work that has identified upwelling as the primary driver of productivity changes in the EEP/EEEP (Costa et al., 2016, 2017; Jacobel et al., 2019; Pallone et al., 2025; Rafter et al., 2017; Winckler et al., 2016), rather than dust-driven Fe fertilization. Additional evidence in support of the far-field influence of the SO can be found in the spectral analysis (Note S2 in Supporting Information S1) of our Ba_{xs} flux and the $^{231}Pa/^{230}Th$ data (Figure 5). The power spectral density for both productivity proxies shows the influence of the 41-kyr obliquity signal, which originates at high latitudes and is likely the signature of excess nutrients exported from the Southern Ocean related to obliquity forcing (Ai et al., 2020). The spectral data also show the signature of orbital precession, again suggestive of upwelling, but because orbital precession influences upwelling dynamics in both the SO and equatorial Pacific, it is challenging to parse the relative contributions of local versus distal processes to the power observed in the precession band. Overall, the evidence for power concentrated at orbital frequencies strongly supports the role of local and SO upwelling, not dust, in delivering nutrients and driving productivity in the equatorial Pacific.

5.2.2. Intercomparison of Productivity Proxies

While there is significant shared variability between $^{231}Pa/^{230}Th$ and Ba_{xs} fluxes (Figure 4), a direct comparison of the two records (Figure 6) reveals interesting differences that are not immediately apparent in the time series data (Figure 4 panels E and F). The r^2 between the data sets at Site 1240 (no interpolation, quantified to 130 ka) is 0.087, $p = 0.055$. Comparing this relationship to previously published results from the CEP (Costa et al., 2016) shows that the strength of the relationship at ODP 1240 is significantly weaker than expected relative to the CEP ($r^2 = 0.85$ $p < 0.01$), although the latter data set is restricted to timeslice coverage from 0–10 ka to 17–27 ka. However, considering the data from across the equatorial Pacific as a whole, there seems to be good agreement in the relationship between Ba_{xs} flux and $^{231}Pa/^{230}Th$ ($r^2 = 0.81$, $p < 0.05$). Examining the relationship between Ba_{xs} flux (Loveley et al., 2017) and $^{231}Pa/^{230}Th$ (Schimmenti et al., 2022) at site 17JC, also in the EEEP, adds further nuance to the intercomparison (Figure S2 in Supporting Information S1). The coefficient of determination between the two data sets at 17JC is $r^2 = 0.065$, $p = 0.01$ (no data interpolation, data extend to 25 ka only) and the slope of the relationship between Ba_{xs} flux and $^{231}Pa/^{230}Th$ is actually negative, driven by very high Ba_{xs} fluxes (up to 9.7 mg/cm^2/kyr) and $^{231}Pa/^{230}Th$ ratios that appear to reach a maximum value of ~0.2 during the early deglacial.

A weakening of the relationship between proxies might reflect a change in the sensitivity of Ba_{xs} fluxes to total organic productivity, or of $^{231}Pa/^{230}Th$ to opal export, or changes in the preservation of either proxy. For Ba_{xs}, changes in preservation might be expected if sulfate reduction, driven by high productivity, had caused the loss of part of the Ba_{xs} signal (Carter et al., 2020). That effect is the opposite of what we see in the EEEP data, where Ba_{xs} fluxes appear to continue to increase while $^{231}Pa/^{230}Th$ ratios remain low, especially from 100 to 130 ka.

Although $^{231}Pa/^{230}Th$ and Ba_{xs} fluxes are proxies for different types of primary production (opal and bulk organic productivity, respectively), they are generally expected to covary as upwelling delivers nutrients to the region and, as demonstrated by our spectral analysis, they do have shared variability at key orbital periodicities. General agreement on the sense of productivity changes might be made noisier (experience a change in slope) if one form of surface productivity was favored over another due to changes in the chemical properties of upwelled water. For

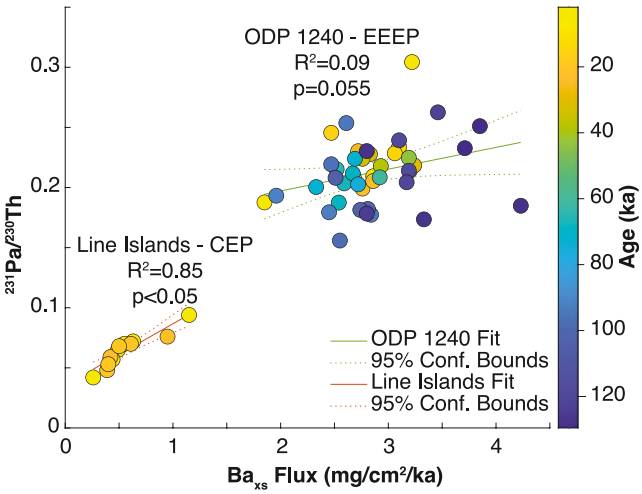

Figure 6. Relationship between Ba_{xs} flux and $^{231}Pa/^{230}Th$ at two equatorial Pacific sites. The color of symbols corresponds to their age, as indicated by the colorbar at right.

example, waters high in nitrogen or phosphorous but low in silica would favor non-siliceous phytoplankton over diatoms and opal production. This may have been the situation during early MIS 5 when Ba_{xs} fluxes are high, but $^{231}Pa/^{230}Th$ ratios are low relative to what might be expected based on the slope of the Line Islands data and ODP 1240 data during MIS 2 (Figure 6). Although the unusually weak relationship between the productivity proxies in the EEEP is worthy of further investigation, the conclusions that follow about bottom water oxygen are not dependent upon the choice of export indicator and we consider both proxies in tandem moving forward.

5.3. Bottom Water Oxygen

Bottom water oxygen is an important paleoceanographic variable both for its significance for organisms that have aerobic metabolisms, as well as for its stoichiometric relationship with deep sea respired carbon concentrations. Figure 7 depicts four proxies for bottom water oxygen that have been measured at ODP 1240. Authigenic uranium (aU) (Jacobel et al., 2020; Pallone et al., 2025) shows qualitative trends in BWO, U/Ba suggests quantitative variations, $\Delta\delta^{13}C$ provides a semi-quantitative BWO reconstruction that can be considered an upper bound on concentrations, and finally our new qualitative Mn/Al-based reconstruction. Despite the different sedimentary constituents that are responsible for reflecting BWO in each of these reconstructions, the overall sense of variability is markedly similar, giving confidence in the shared features of the reconstruction.

Obtaining proxy constraints on BWO has been a challenge because co-occurring changes in organic carbon fluxes can also drive local redox changes, which are recorded by each proxy to a different extent. To identify changes in BWO that are due to basin-wide changes in oxygen and respired carbon storage, we compare our proxy reconstructions to our co-registered records of Ba_{xs} flux and $^{231}Pa/^{230}Th$ (Figure 7). The most striking features of the Ba_{xs} flux record are the deglacial increase in productivity beginning around 140 ka and the peak at ~50 ka. For $^{231}Pa/^{230}Th$, the highest ratios are observed at ~50 ka and the last deglaciation. Deglacial increases in productivity actually coincide with intervals of oxygenation (the opposite of what might be expected given enhanced abyssal respiration in response to organic carbon rain) and we see only a weak response of BWO to the 50 ka event. A correlation matrix for the two productivity proxies and the four BWO proxies is provided in Table S1 of Supporting Information S1, spanning the full length of the records. The only BWO and productivity proxy relationship that shows an R^2 value above 0.1 is between Ba_{xs} flux and aU, which we do not consider to be a quantitative proxy for BWO precisely because it is so susceptible to the influence of organic carbon. This comparison gives us confidence that the features of the BWO record reflect the primary influence of deep Pacific Ocean chemistry rather than local organic carbon flux, and permits us to proceed with interpretation of the BWO records as representative of regional, rather than local, BWO.

Bottom water oxygen was low through glacial MIS 6 (low O_2 inferred from aU, U/Ba, and Mn/Al), and increased rapidly during TII (peak in Mn/Al at 130 ka, step change in U/Ba and aU) into MIS 5e. Peak BWO values during MIS5e, as recorded by U/Ba and $\Delta\delta^{13}C$, are both within uncertainty of their respective reconstructed Holocene concentrations and U/Ba values are within uncertainty of modern BWO measurements of ~110 μmol/kg (Suzuki et al., 2013). U/Ba and $\Delta\delta^{13}C$ disagree about the absolute value of MIS 5e BWO, with $\Delta\delta^{13}C$ suggesting higher oxygen concentrations, likely due to a potential bias of the proxy that has previously been observed and attributed to the influence of sedimentary denitrification on the $\delta^{13}C$ of the infaunal benthic foraminifera that comprises an important part of the proxy reconstruction (Jacobel et al., 2020; Lu et al., 2023).

The peak in MIS 5e BWO may have been short-lived, as aU, $\Delta\delta^{13}C$, and Mn/Al suggest a decrease in BWO into MIS 5b. The timing of this BWO decrease coincides with a decrease in productivity seen in the Ba_{xs} flux and $^{231}Pa/^{230}Th$, which, other variables held constant, would be expected to *raise* local BWO. This lends confidence to the interpretation of high MIS5e BWO decreasing into MIS 5b as a regional feature, although the decrease is not apparent in the U/Ba record. Whether or not BWO declined after the peak of the last interglacial, BWO remained above MIS 6 values throughout the duration of MIS 5 (all records). Substage variability is apparent during MIS 5 with peaks in U/Ba, $\Delta\delta^{13}C$, and Mn/Al at ~116 ka (during MIS 5e) and peaks in aU, U/Ba, and Mn/

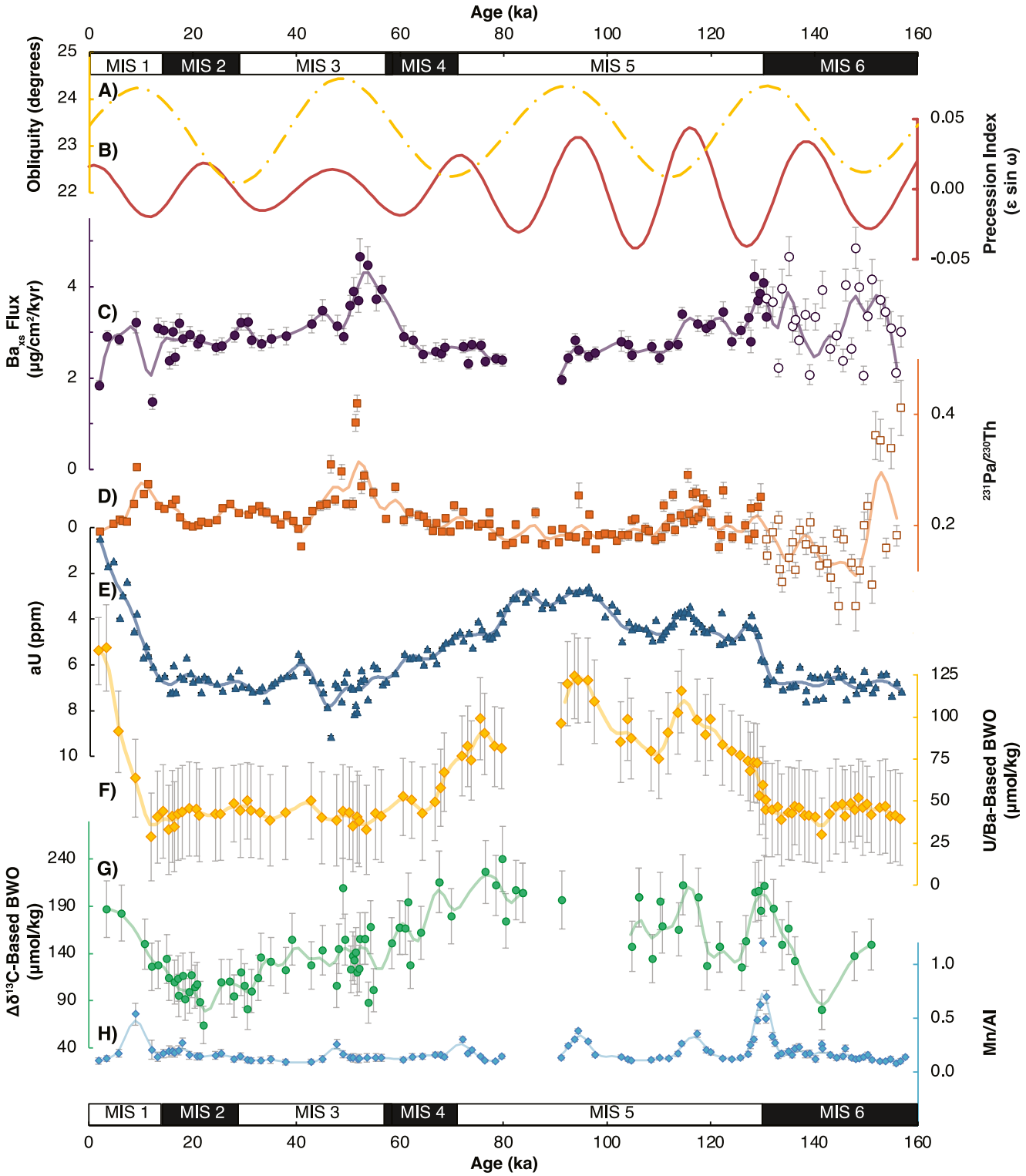

Figure 7. Local productivity context and proxies for bottom water oxygen (BWO) in the EEEP. (a) Obliquity (dashed yellow line), (b) Precession index (solid red line), (c) Ba_{xs} flux from ODP 1240 (purple circles), (d) $^{231}Pa/^{230}Th$ (Pallone et al., 2025) (orange squares) (e) authigenic uranium (inverted scale; blue triangles) (Jacobel et al., 2020; Pallone et al., 2025), (f) U/Ba-based BWO from ODP 1240 (gold diamonds) (this study, Jacobel et al., 2020; Costa et al., 2023), (g) $\Delta\delta^{13}C$-based BWO reconstruction from ODP 1240 (teal circles) (Jacobel et al., 2020) using the calibration of Hoogakker et al., 2025, and (h) Mn/Al ratios from ODP 1240 (blue diamonds). Open symbols in a, b represent flux-normalized data older than 130 ka which have large uncertainties (Note S1 in Supporting Information S1). All error bars reflect one sigma uncertainties.

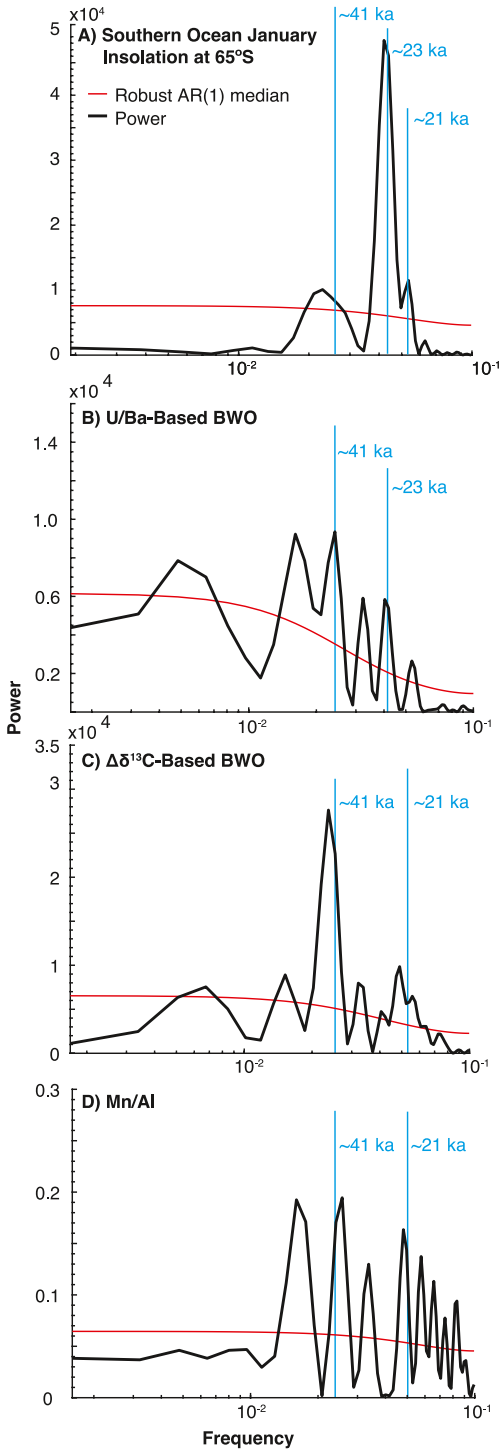

Figure 8. Spectral analysis of (a) Southern Ocean Insolation at 65°S, (b) U-Ba based BWO, (c) $\Delta\delta^{13}$C-based BWO, and (d) Mn/Al ratios. Black lines show the power spectra of the time series, the red line is the AR(1) spectrum, and blue lines indicate peaks of power that coincide with orbital periodicities.

Al at 95 ka (close to the peak of MIS 5c). There is a gap in the $\Delta\delta^{13}$C during MIS 5b-c due to low *Globobulimina spp.* abundances (potentially due to high BWO), and the ash layer at ~80 ka interrupts the U/Ba and Mn/Al records. Peak MIS 5a values may also have occurred ~72–75 ka (aU, U/Ba, $\Delta\delta^{13}$C, and Mn/Al).

The peak of MIS 5a was followed by a long term decline in BWO concentrations, with values showing a consistent decrease by 70 ka, marking the end of elevated MIS5 BWO concentrations (all proxies). Decreases in BWO concentrations to the fully glacial state may have been reached by 54 ka (U/Ba), although $\Delta\delta^{13}$C suggests that values continued to decrease through the peak of the LGM at 23 ka. MIS 2/3 glacial BWO concentrations appear very similar relative to the reconstruction of MIS 6 levels (U/Ba and $\Delta\delta^{13}$C). There is some disagreement between the proxies about the timing of TI reoxygenation of the deep ocean, with $\Delta\delta^{13}$C showing the earliest onset at 23 ka, aU indicating a change at 16 ka, and U/Ba and Mn/Al showing changes starting at ~14 ka. Given that aU and thus U/Ba can be susceptible to postdepositional remobilization (burndown) during deglacial porewater reoxygenation (Jacobel et al., 2017b, 2020), they would tend to record an older deglacial timing relative to the other proxies we employ here. We consider Mn/Al to be the most conservative and reliable indicator of the timing of deglacial reoxygenation because preservation of the deglacial Mn peak would be expected to occur when porewaters become more oxic. The position of the Mn/Al peak in the sediment cannot be modified by post-depositional processes other than those which would serve to remove it, which has clearly not happened at ODP 1240. The timing of reoxygenation provided by the deglacial Mn/Al peak is in good agreement with the youngest deglacial authigenic Mn peak observed in equatorial Pacific sediments at 11 ka, reconstructed at TT013-PC72 (0.1°N, 139.4°W, 4,298 m) (Pavia et al., 2021).

The timing of MIS 5 BWO maxima and short-lived peaks and troughs in BWO throughout the record are notable because they appear to occur with regular periodicity (Figure 7), suggestive of a relationship with orbital precession and/or obliquity. Indeed, spectral analysis shows power at the frequency associated with both obliquity and precession in the U/Ba, $\Delta\delta^{13}$C, and Mn/Al records (Figure 8). It is important to consider whether these short-lived peaks and troughs in BWO might be driven by local productivity, especially since we previously identified orbital-scale variability in both our Ba_{xs} flux and $^{231}Pa/^{230}Th$ records (Figure 5). Indeed, we do not present the power spectral density (PSD) for aU in Figure 8 because of the potential influence of productivity on the magnitude of the proxy response and thus the spectral character (although the PSD for aU does show the influence of obliquity). When evaluating the relationship between productivity and BWO, it is important to keep in mind the directionality of influence, specifically that increasing (decreasing) productivity might be expected to drive the appearance of lower (higher) bottom water oxygen concentrations. We carried out a windowed correlation analysis for Mn/Al regressed against Ba_{xs} fluxes for the time intervals 124–139, 110–121, 90–98, 66–77, 42–57 and 9–21 ka. With the exception of the productivity peak from 42 to 57 ka, the slopes of each of these intervals were near zero or slightly positive, which is to say local organic carbon fluxes were not responsible for driving the apparent increases in Mn/Al during these intervals. We did observe a statistically significant negative relationship between the Mn/Al proxy for BWO and Ba_{xs} fluxes during the interval 42–57 ka. This does not necessarily mean that bottom waters were not regionally more oxic during this interval, but rather that we cannot definitively rule out that locally decreasing productivity from the

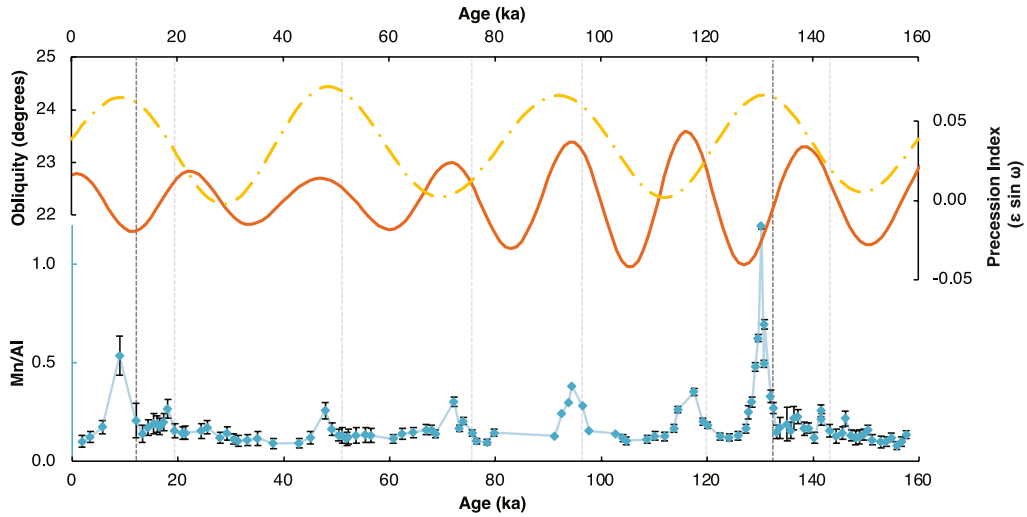

Figure 9. Obliquity (dashed gold line), precession (solid orange line) and deep Pacific BWO changes as illustrated by Mn/Al ratios (blue diamonds and line). The thin gray lines indicate that the onset of BWO increases. The thick gray lines indicate the onset of BWO maxima that correspond to deglacial transitions.

export flux peak ~53 ka led these proxies to record an increase in BWO oxygenation. In sum, with the exception of the productivity peak around ~53 ka, the apparent precessional variability in BWO concentrations can be robustly attributed to upstream changes in ocean ventilation. Given that NPDW is not thought to have experienced direct changes in ventilation on glacial-interglacial timescales (Jaccard & Galbraith, 2013), the generally low productivity of the mid-latitude North Pacific, and the absence of productivity peaks that correspond with glacial/interglacial cyclicity (Costa et al., 2018), we suggest that the most likely upstream region influencing deep equatorial Pacific oxygenation is in the Southern Ocean, where NPDW originates as AABW.

The signatures of obliquity and precession have not been previously reconstructed in deep Pacific Ocean oxygen concentrations (Figures 7 and 8), providing an opportunity to draw new inferences about the mechanistic forcing (s). BWO oxygenation events as illustrated by Mn/Al ratios (which we argue have the best temporal fidelity) are a poor match for local equatorial insolation at 0°N as might be expected since we have rigorously ruled out local influences on our BWO records for all but potentially the event at ~53 ka. Instead, increases in BWO that are not associated with terminations appear to correspond with an increasing index of precession, associated with increasing January (austral summer) insolation in the Southern Ocean (Figure 9). Orbital precession drives changes in Southern Ocean air-sea interactions (Persch et al., 2023), because of a seasonally asymmetric response of the Southern Hemisphere Westerly Winds (SWW) to changes in insolation. Precession maxima cause the SWW to shift southward during austral summer and fall (Persch et al., 2023). The reconstruction of 41 kyr periodicity in all three BWO records (Figure 8) is also consistent with obliquity forcing (low at 110 and 70 ka) driving southward shifted SWW (Ai et al., 2020; Timmermann et al., 2014).

Although upwelling at the latitude of the SWW is not expected to directly influence deepwater formation, strengthening of the SWW is associated with a weakening of the Polar Easterlies (Bracegirdle et al., 2008; Hazel & Stewart, 2019; Menviel & Spence, 2024; Neme et al., 2022; Spence et al., 2014). In turn, weaker Polar Easterlies have been associated with increased Antarctic Bottom Water (AABW) formation (Gordon et al., 2015; Hazel & Stewart, 2019; Menviel & Spence, 2024; Silvano et al., 2020; Stewart & Thompson, 2012, 2013) and bottom water ventilation (Matear et al., 2000; Orsi & Wiederwohl, 2009). Specifically, weaker easterlies transport less sea ice into AABW formation regions (like the Ross and Weddell Seas) allowing for greater polynya activity (Schmidt et al., 2023; Silvano et al., 2020) and greater export of oxygen-rich dense waters off the shelf (Matear et al., 2000; Orsi & Wiederwohl, 2009) which contribute to AABW (Schmidt et al., 2023). In sum, our new results show that orbital forcing of the Southern Ocean can be linked to changes in deep ocean ventilation with implications for the global distribution of bottom water oxygen and respired carbon storage.

Our new multi-proxy reconstructions of deep Pacific BWO are consistent with previous reconstructions, but also reveal important new information about basin-wide deepwater chemistry. First, deep Pacific BWO levels

of ∼50 μmol/kg (based on U/Ba) appear to characterize the last two glacial maxima, indicating enhanced respired carbon storage during successive glacial periods. Second, deglacial ventilation of deep water masses, releasing respired CO_2 and replenishing dissolved oxygen concentrations, is a consistent feature of the last two terminations. Manganese peaks in central equatorial Pacific sediments suggest that this relationship extends back at least a million years (Pavia et al., 2021). Previous work associated deglacial increases in deep ocean ventilation with orbital forcing in the Northern Hemisphere (Denton et al., 2010) initiating ocean-atmosphere changes that drive changes in Southern Ocean overturning including southward shifted westerly winds (Toggweiler et al., 2006), which enhance upwelling (Ai et al., 2020; Anderson et al., 2009), ventilate bottom waters (Gottschalk et al., 2016; Jaccard et al., 2016), and release CO_2. Third, bottom water oxygen availability in the deep Pacific during the last interglacial (MIS 5) appears to have peaked around 95 ka, near modern concentrations, with subsequent decreases indicative of BWO depletion, and associated enhanced respired carbon storage, occurring after the onset of the last glacial inception at ∼115 ka (Bereiter et al., 2015). Finally, the enhanced resolution of these new bottom water oxygen records suggests that not only is insolation key for pacing glacial-interglacial cycles, but that orbital precession and obliquity, acting via physical processes in the Southern Ocean, play a previously unappreciated but important role in changing deep ocean storage of dissolved oxygen and respired carbon.

6. Conclusions

This paper presents new records of Ba_{xs} flux as a proxy for organic carbon export to the seafloor, and evaluates new records of Mn/Al, and U/Ba (Costa et al., 2023), alongside previously published $\Delta\delta^{13}C$ (Jacobel et al., 2020), and aU (Jacobel et al., 2020; Pallone et al., 2025) data as proxies for bottom water oxygen. Evaluating the Ba_{xs} concentration data in comparison with flux-normalized Ba_{xs} data reinforces the critical importance of flux normalization (see review in Costa et al., 2020) for accurate interpretation of the export production record. Concentration and flux-normalized data sets show opposite trends in glacial-interglacial productivity change, and features of the concentration data set that reoccur on ∼20 ka timescales appear to be heavily influenced by variable dilution by calcium carbonate dissolution. Our findings illustrate the crucial importance of flux normalizing data when interpreting proxy records in regions where the flux of sedimentary constituents and/or their preservation is highly variable.

Our new Ba_{xs} flux record reveals changes in easternmost equatorial Pacific export production over the last ∼160 ka that are consistent with more spatially comprehensive but temporally limited assessments of glacial-interglacial and deglacial productivity patterns over the last glacial cycle (Costa et al., 2017a). The Ba_{xs} fluxes show comparable glacial and interglacial export production with deglacial productivity peaks (and a peak at ∼53 ka) that are consistent with obliquity and precession-forced changes in Southern Ocean nutrient delivery via oceanic tunneling (Ai et al., 2020; Costa et al., 2017a; Hayes et al., 2011; Pallone et al., 2025; Pena et al., 2008). Importantly, our Ba_{xs} flux record has some differences from a previously published $^{231}Pa/^{230}Th$ reconstruction from the same site (Pallone et al., 2025), specifically higher Ba_{xs} fluxes during TII. We suggest that both proxies provide important and potentially distinct perspectives on export flux as they reflect different components of primary productivity.

We use both the Ba_{xs} flux and the $^{231}Pa/^{230}Th$ proxies for export flux to inform our interpretation of BWO proxies in the easternmost equatorial Pacific. We find strong evidence that changes in BWO at ODP 1240 are driven by basin-scale processes, not local changes in organic carbon supply and sedimentary respiration, and we interpret the multiproxy BWO reconstruction as indicative of changes in oxygen and respired carbon storage that are primarily driven by processes in the Southern Ocean. While the observed glacial decrease in BWO and increase in respired carbon are consistent with previously published results, our finding of BWO variability corresponding with both obliquity and precession is a new observation. We suggest that this variability is likely driven by local obliquity minima and precession maxima that force southerly shifts in the Southern Hemisphere Westerly Winds, resulting in weaker Polar Easterlies, enhanced AABW formation and better ventilated deep waters. These results suggest a previously under-appreciated role for orbital obliquity and precession as drivers of oxygen availability and respired carbon storage in Earth's oceans and may also have important implications for predictions of future ocean chemistry as the SWW intensify and shift southwards (Perren et al., 2020) under conditions of anthropogenic climate forcing.

Conflict of Interest

The authors declare no conflicts of interest relevant to this study.

Data Availability Statement

All authors contributed to data collection and the final manuscript. Work was conceived by A.W.J., R.F.A., and J.F.M. Data were analyzed by A.W.J. The manuscript was written by A.W.J. with contributions from all coauthors. The Ba, Ba_{xs}, Fe, Al, Mn, and ln(U/Ba) data used for reconstruction of bottom water oxygen conditions in the study (Jacobel et al., 2025) are available at the National Oceanic and Atmospheric Administration (NOAA) National Centers for Environmental Information (NCEI) data repository via [https://doi.org/10.25921/amyj-ew81]. The data can also be accessed via PANGAEA at https://doi.pangaea.de/10.1594/PANGAEA.982869.

Acknowledgments
This work was supported in part by NSF OCE-210300 to A.W.J., NSF OCE-2103031 to K.M.C., NSF AGS-1502889 to J.F.M., and startup funding to A.W.J. from Middlebury College.

References

Ai, X. E., Studer, A. S., Sigman, D. M., Martínez-García, A., Fripiat, F., Thöle, L. M., et al. (2020). Southern Ocean upwelling, Earth's obliquity, and glacial-interglacial atmospheric CO_2 change. *Science*, *370*(6522), 1348–1352. https://doi.org/10.1126/science.abd2115

Anderson, R. F., Ali, S., Bradtmiller, L. I., Nielsen, S. H. H., Fleisher, M. Q., Anderson, B. E., & Burckle, L. H. (2009). Wind-driven upwelling in the Southern Ocean and the Deglacial rise in atmospheric CO_2. *Science*, *323*(5920), 1443–1448. https://doi.org/10.1126/science.1167441

Anderson, R. F., Bacon, M. P., & Brewer, P. G. (1983). Removal of ^{230}Th and ^{231}Pa from the open ocean. *Earth and Planetary Science Letters*, *62*(1), 7–23. https://doi.org/10.1016/0012-821X(83)90067-5

Anderson, R. F., Fleisher, M. Q., Lao, Y., & Winckler, G. (2008). Modern $CaCO_3$ preservation in equatorial Pacific sediments in the context of late-Pleistocene glacial cycles. *Marine Chemistry*, *111*(1–2), 30–46. https://doi.org/10.1016/j.marchem.2007.11.011

Anderson, R. F., Sachs, J. P., Fleisher, M. Q., Allen, K. A., Yu, J., Koutavas, A., & Jaccard, S. L. (2019). Deep-Sea oxygen depletion and ocean carbon sequestration during the last ice age. *Global Biogeochemical Cycles*, *33*(3), 301–317. https://doi.org/10.1029/2018GB006049

Beaufort, L., de Garidel-Thoron, T., Mix, A. C., & Pisias, N. G. (2001). ENSO-Like forcing on oceanic primary production during the late Pleistocene. *Science*, *293*(5539), 2440–2444. https://doi.org/10.1126/science.293.5539.2440

Bereiter, B., Eggleston, S., Schmitt, J., Ahles, C. N., Stocker, T. F., Fischer, H., et al. (2015). Revision of the EPICA Dome C CO_2 record from 800 to 600 kyr before present. *Geophysical Research Letters*, *42*(2), 542–549. https://doi.org/10.1002/2014GL061957

Berger, W. H., Finkel, R. C., Killingley, J. S., & Marchig, V. (1983). Glacial–Holocene transition in deep-sea sediments: Manganese-spike in the East-Equatorial Pacific. *Nature*, *303*(5914), 231–233. https://doi.org/10.1038/303231a0

Bischoff, T., Schneider, T., & Meckler, A. N. (2017). A conceptual model for the response of tropical rainfall to orbital variations. *Journal of Climate*, *30*(20), 8375–8391. https://doi.org/10.1175/JCLI-D-16-0691.1

Boyle, E. A. (1990). Quaternary deepwater paleoceanography. *Science*, *249*(4971), 863–870. https://doi.org/10.1126/science.249.4971.863

Bracegirdle, T. J., Connolley, W. M., & Turner, J. (2008). Antarctic climate change over the twenty first century. *Journal of Geophysical Research*, *113*(D3). https://doi.org/10.1029/2007JD008933

Bradbury, H. J., Thomas, N. C., Mleneck-Vautravers, M., & Hodell, D. A. (2024). Revisiting the relationship between the pore water carbon isotope gradient and bottom water oxygen concentrations. *Geochimica et Cosmochimica Acta*, *366*, 84–94. https://doi.org/10.1016/j.gca.2023.12.011

Bradtmiller, L. I., Anderson, R. F., Sachs, J. P., & Fleisher, M. Q. (2010). A deeper respired carbon pool in the glacial equatorial Pacific Ocean. *Earth and Planetary Science Letters*, *299*(3–4), 417–425. https://doi.org/10.1016/j.epsl.2010.09.022

Calvert, S. E., & Pedersen, T. F. (1996). Sedimentary geochemistry of manganese; implications for the environment of formation of manganiferous black shales. *Economic Geology (Lancaster, Pa.)*, *91*(1), 36–47. https://doi.org/10.2113/gsecongeo.91.1.36

Calvo, E., Pelejero, C., Pena, L. D., Cacho, I., & Logan, G. A. (2011). Eastern Equatorial Pacific productivity and related-CO_2 changes since the last glacial period. *Proceedings of the National Academy of Sciences*, *108*(14), 5537–5541. https://doi.org/10.1073/pnas.1009761108

Canfield, D. E. (1994). Factors influencing organic carbon preservation in marine sediments. *Chemical Geology*, *114*(3–4), 315–329. https://doi.org/10.1016/0009-2541(94)90061-2

Carter, S. C., Paytan, A., & Griffith, E. M. (2020). Toward an improved understanding of the marine barium cycle and the application of marine barite as a paleoproductivity proxy. *Minerals (Basel)*, *10*(5), 421. https://doi.org/10.3390/min10050421

Chase, Z., Anderson, R. F., Fleisher, M. Q., & Kubik, P. W. (2002). The influence of particle composition and particle flux on scavenging of Th, Pa and Be in the ocean. *Earth and Planetary Science Letters*, *204*(1–2), 215–229. https://doi.org/10.1016/S0012-821X(02)00984-6

Chase, Z., Anderson, R. F., Fleisher, M. Q., & Kubik, P. W. (2003). Scavenging of ^{230}Th, ^{231}Pa and ^{10}Be in the Southern Oceanocean (SW Pacific sector): The importance of particle flux, particle composition and advection. *Deep Sea Research Part II: Topical Studies in Oceanography*, *50*(3–4), 739–768. https://doi.org/10.1016/S0967-0645(02)00593-3

Clement, A. C., Hall, A., & Broccoli, A. J. (2004). The importance of precessional signals in the tropical climate. *Climate Dynamics*, *22*(4), 327–341. https://doi.org/10.1007/s00382-003-0375-8

Clement, A. C., Seager, R., & Cane, M. A. (1999). Orbital controls on the El Niño/southern oscillation and the tropical climate. *Paleoceanography*, *14*(4), 441–456. https://doi.org/10.1029/1999PA900013

Clement, A. C., Seager, R., & Cane, M. A. (2000). Suppression of El Niño during the mid-Holocene by changes in the Earth's orbit. *Paleoceanography*, *15*(6), 731–737. https://doi.org/10.1029/1999PA000466

Costa, K. M., Anderson, R. F., McManus, J. F., Winckler, G., Middleton, J. L., & Langmuir, C. H. (2018). Trace element (Mn, Zn, Ni, V) and Authigenic Uranium (AU) geochemistry reveal sedimentary redox history on the Juan de Fuca Ridge, North Pacific Ocean. *Geochimica et Cosmochimica Acta*, *236*, 79–98. https://doi.org/10.1016/j.gca.2018.02.016

Costa, K. M., Hayes, C. T., Anderson, R. F., Pavia, F. J., Bausch, A., Deng, F., et al. (2020). ^{230}Th normalization: New insights on an essential tool for quantifying sedimentary fluxes in the modern and quaternary ocean. *Paleoceanography and Paleoclimatology*, *35*(2), e2019PA003820. https://doi.org/10.1029/2019PA003820

Costa, K. M., Jacobel, A. W., McManus, J. F., Anderson, R. F., Winckler, G., & Thiagarajan, N. (2017). Productivity patterns in the equatorial Pacific over the last 30,000 years. *Global Biogeochemical Cycles*, *31*(5), 850–865. https://doi.org/10.1002/2016GB005579

Costa, K. M., McManus, J. F., Anderson, R. F., Ren, H., Sigman, D. M., Winckler, G., et al. (2016). No iron fertilization in the equatorial Pacific Ocean during the last ice age. *Nature*, *529*(7587), 519–522. https://doi.org/10.1038/nature16453

Costa, K. M., Nielsen, S. G., Wang, Y., Lu, W., Hines, S. K. V., Jacobel, A. W., & Oppo, D. W. (2023). Marine sedimentary uranium to barium ratios as a potential quantitative proxy for Pleistocene bottom water oxygen concentrations. *Geochimica et Cosmochimica Acta*, *343*, 1–16. https://doi.org/10.1016/j.gca.2022.12.022

de la Fuente, M., Skinner, L., Calvo, E., Pelejero, C., & Cacho, I. (2015). Increased reservoir ages and poorly ventilated deep waters inferred in the glacial Eastern Equatorial Pacific. *Nature Communications*, *6*(1), 7420. https://doi.org/10.1038/ncomms8420

Denton, G. H., Anderson, R. F., Toggweiler, J. R., Edwards, R. L., Schaefer, J. M., & Putnam, A. E. (2010). The last glacial termination. *Science*, *328*(5986), 1652–1656. https://doi.org/10.1126/science.1184119

Drexler, J. W., Rose, W. I., Sparks, R. S. J., & Ledbetter, M. T. (1980). The Los Chocoyos ash, Guatemala: A major stratigraphic marker in Middle America and in three ocean basins. *Quaternary Research*, *13*(3), 327–345. https://doi.org/10.1016/0033-5894(80)90061-7

Drysdale, R. N., Drysdale, R. N., Hellstrom, J. C., Zanchetta, G., Zanchetta, G., Fallick, A. E., et al. (2009). Evidence for obliquity forcing of glacial termination II. *Science*, *325*(5947), 1527–1531. https://doi.org/10.1126/science.1170371

Dymond, J., & Collier, R. (1996). Particulate barium fluxes and their relationships to biological productivity. *Deep Sea Research Part II: Topical Studies in Oceanography*, *43*(4–6), 1283–1308. https://doi.org/10.1016/0967-0645(96)00011-2

Dymond, J., Seuss, E., & Lyle, M. (1992). Barium in deep-sea sediment: A geochemical proxy for paleoproductivity. *Paleoceanography*, *7*(2), 163–181. https://doi.org/10.1029/92PA00181

Endrizzi, F., & Rao, L. (2014). Chemical speciation of uranium (VI) in marine environments: Complexation of calcium and magnesium ions with $[(UO_2)(CO_3)^3]^{4-}$ and the effect on the extraction of uranium from seawater. *Chemistry—A European Journal*, *20*(44), 14499–14506. https://doi.org/10.1002/chem.201403262

Erb, M. P., Broccoli, A. J., Graham, N. T., Clement, A. C., Wittenberg, A. T., & Vecchi, G. A. (2015). Response of the equatorial Pacific seasonal cycle to orbital forcing. *Journal of Climate*, *28*(23), 9258–9276. https://doi.org/10.1175/JCLI-D-15-0242.1

Falkner, K. K., klinkhammer, G. P., Bowers, T. S., Todd, J. F., Lewis, B. L., Landing, W. M., & Edmond, J. M. (1993). The behavior of barium in anoxic marine waters. *Geochimica et Cosmochimica Acta*, *57*(3), 537–554. https://doi.org/10.1016/0016-7037(93)90366-5

Fiedler, P. C., & Talley, L. D. (2006). Hydrography of the eastern tropical Pacific: A review. *Progress in Oceanography, A Review of Eastern Tropical Pacific Oceanography*, *69*(2–4), 143–180. https://doi.org/10.1016/j.pocean.2006.03.008

François, R., Bacon, M. P., Altabet, M. A., & Labeyrie, L. D. (1993). Glacial/interglacial changes in sediment rain rate in the SW Indian sector of subantarctic waters as recorded by ^{230}Th, ^{231}Pa, U, and? ^{15}N. *Paleoceanography*, *8*(5), 611–629. https://doi.org/10.1029/93PA00784

François, R., Frank, M., Rutgers van der Loeff, M., Bacon, M. P., Geibert, W., Kienast, S., et al. (2007). Comment on "Do geochemical estimates of sediment focusing pass the sediment test in the equatorial Pacific? In. M. Lyle, N. Mitchell, N. Pisias, A. Mix, J. Ignacio Martinez, & A. Paytan (Eds.), *Paleoceanography*, (Vol. 22). https://doi.org/10.1029/2005PA001235

François, R., Honjo, S., Manganini, S. J., & Ravizza, G. E. (1995). Biogenic barium fluxes to the deep sea: Implications for paleoproductivity reconstruction. *Global Biogeochemical Cycles*, *9*(2), 289–303. https://doi.org/10.1029/95GB00021

Froelich, P. N., Klinkhammer, G. P., Bender, M. L., Luedtke, N. A., Heath, G. R., Cullen, D., et al. (1979). Early oxidation of organic matter in pelagic sediments of the eastern equatorial Atlantic: Suboxic diagenesis. *Geochimica et Cosmochimica Acta*, *43*(7), 1075–1090. https://doi.org/10.1016/0016-7037(79)90095-4

Garcia, H. E., Bouchard, C., Cross, S. L., Paver, C. R., Wang, Z., Reagan, J. R., et al. (2023). *World Ocean Atlas 2023, volume 4: Dissolved inorganic nutrients (phosphate, nitrate, silicate). A. Mishonov, Tech*. NOAA Atlas NESDIS 92. https://doi.org/10.25923/39qw-7j08

Gordon, A. L., Huber, B. A., & Busecke, J. (2015). Bottom water export from the western Ross Sea, 2007 through 2010. *Geophysical Research Letters*, *42*(13), 5387–5394. https://doi.org/10.1002/2015GL064457

Gottschalk, J., Skinner, L. C., Lippold, J., Vogel, H., Frank, N., Jaccard, S. L., & Waelbroeck, C. (2016). Biological and physical controls in the Southern Ocean on past millennial-scale atmospheric CO_2 changes. *Nature Communications*, *7*(1), 11539. https://doi.org/10.1038/ncomms11539

Hans Wedepohl, K. (1995). The composition of the continental crust. *Geochimica et Cosmochimica Acta*, *59*(7), 1217–1232. https://doi.org/10.1016/0016-7037(95)00038-2

Hayes, C. T., Anderson, R. F., & Fleisher, M. Q. (2011). Opal accumulation rates in the equatorial Pacific and mechanisms of deglaciation. *Paleoceanography*, *26*(1). https://doi.org/10.1029/2010PA002008

Hayes, C. T., Anderson, R. F., Fleisher, M. Q., Serno, S., Winckler, G., & Gersonde, R. (2014). Biogeography in ^{231}Pa/^{230}Th ratios and a balanced ^{231}Pa budget for the Pacific Ocean. *Earth and Planetary Science Letters*, *391*, 307–318. https://doi.org/10.1016/j.epsl.2014.02.001

Hayes, C. T., Anderson, R. F., Fleisher, M. Q., Vivancos, S. M., Lam, P. J., Ohnemus, D. C., et al. (2015). Intensity of Th and Pa scavenging partitioned by particle chemistry in the North Atlantic Ocean. *Marine Chemistry*, *170*, 49–60. https://doi.org/10.1016/j.marchem.2015.01.006

Hayes, C. T., Costa, K. M., Anderson, R. F., Calvo, E., Chase, Z., Demina, L. L., et al. (2021). Global Ocean sediment composition and burial flux in the deep sea. *Global Biogeochemical Cycles*, *35*(4), e2020GB006769. https://doi.org/10.1029/2020GB006769

Hazel, J. E., & Stewart, A. L. (2019). Are the near-Antarctic easterly winds weakening in response to enhancement of the Southern Annular Mode? *Journal of Climate*, *32*(6), 1895–1918. https://doi.org/10.1175/JCLI-D-18-0402.1

Henderson, G. M., & Anderson, R. F. (2003). The U-series toolbox for paleoceanography. *Reviews in Mineralogy and Geochemistry*, *52*(1), 493–531. https://doi.org/10.2113/0520493

Hoogakker, B. A. A., Davis, C., Wang, Y., Kusch, S., Nilsson-Kerr, K., Hardisty, D. S., et al. (2025). Reviews and syntheses: Review of proxies for low-oxygen paleoceanographic reconstructions. *Biogeosciences*, *22*(4), 863–957. https://doi.org/10.5194/bg-22-863-2025

Hoogakker, B. A. A., Elderfield, H., Schmiedl, G., McCave, I. N., & Rickaby, R. E. M. (2015). Glacial–interglacial changes in bottom-water oxygen content on the Portuguese margin. *Nature Geoscience*, *8*(1), 40–43. https://doi.org/10.1038/ngeo2317

Hoogakker, B. A. A., Lu, Z., Umling, N., Jones, L., Zhou, X., Rickaby, R. E. M., et al. (2018). Glacial expansion of oxygen-depleted seawater in the eastern tropical Pacific. *Nature*, *562*(7727), 410–413. https://doi.org/10.1038/s41586-018-0589-x

Ivanova, E. V., Beaufort, L., Vidal, L., & Kucera, M. (2012). Precession forcing of productivity in the Eastern Equatorial Pacific during the last glacial cycle. *Quaternary Science Reviews*, *40*, 64–77. https://doi.org/10.1016/j.quascirev.2012.02.020

Jaccard, S. L., & Galbraith, E. D. (2013). Direct ventilation of the North Pacific did not reach the deep ocean during the last deglaciation. *Geophysical Research Letters*, *40*(1), 199–203. https://doi.org/10.1029/2012GL054118

Jaccard, S. L., Galbraith, E. D., Martínez-García, A., & Anderson, R. F. (2016). Covariation of deep Southern Ocean oxygenation and atmospheric CO_2 through the last ice age. *Nature*, *530*(7589), 207–210. https://doi.org/10.1038/nature16514

Jaccard, S. L., Galbraith, E. D., Sigman, D. M., Haug, G. H., François, R., Pedersen, T. F., et al. (2009). Subarctic Pacific evidence for a glacial deepening of the oceanic respired carbon pool. *Earth and Planetary Science Letters*, *277*(1–2), 156–165. https://doi.org/10.1016/j.epsl.2008.10.017

Jacobel, A. W., Anderson, R. F., Jaccard, S. L., McManus, J. F., Pavia, F. J., & Winckler, G. (2020). Deep Pacific storage of respired carbon during the last ice age: Perspectives from bottom water oxygen reconstructions. *Quaternary Science Reviews*, *230*, 106065. https://doi.org/10.1016/j.quascirev.2019.106065

Jacobel, A. W., Anderson, R. F., Winckler, G., Costa, K. M., Gottschalk, J., Middleton, J. L., et al. (2019). No evidence for equatorial Pacific dust fertilization. *Nature Geoscience*, *12*(3), 154–155. https://doi.org/10.1038/s41561-019-0304-z

Jacobel, A. W., McManus, J. F., Anderson, R. F., & Winckler, G. (2016). Large Deglacial shifts of the Pacific intertropical convergence zone. *Nature Communications*, *7*(1), 10449. https://doi.org/10.1038/ncomms10449

Jacobel, A. W., McManus, J. F., Anderson, R. F., & Winckler, G. (2017a). Repeated storage of respired carbon in the equatorial Pacific Ocean over the last three glacial cycles. *Nature Communications*, *8*(1), 1727. https://doi.org/10.1038/s41467-017-01938-x

Jacobel, A. W., McManus, J. F., Anderson, R. F., & Winckler, G. (2017b). Climate-related response of dust flux to the central equatorial Pacific over the past 150 kyr. *Earth and Planetary Science Letters*, *457*, 160–172. https://doi.org/10.1016/j.epsl.2016.09.042

Jacobel, A. W., Pallone, C. T., Costa, K. M., Anderson, R. F., & McManus, J. F. (2025). Eastern equatorial Pacific site ODP 1240 major element data over the last 160 kyr [Dataset]. *National Oceanic and Atmospheric Administration (NOAA) National Centers for Environmental Information (NCEI)*. https://doi.org/10.25921/amyj-ew81

Jalihal, C., Bosmans, J. H. C., Srinivasan, J., & Chakraborty, A. (2019). The response of tropical precipitation to Earth's precession: The role of energy fluxes and vertical stability. *Climate of the Past*, *15*(2), 449–462. https://doi.org/10.5194/cp-15-449-2019

Jin, X., Wang, X., Zhou, X., Jiang, X., Qiao, P., & Liu, C. (2024). Precessional forcing of biogeochemical and nutrient cycling in the tropical western Pacific during the late Pleistocene. *Earth and Planetary Science Letters*, *638*, 118759. https://doi.org/10.1016/j.epsl.2024.118759

Karnauskas, K. B., Jakoboski, J., Johnston, T. M. S., Owens, W. B., Rudnick, D. L., & Todd, R. E. (2020). The Pacific equatorial undercurrent in three generations of global climate models and glider observations. *Journal of Geophysical Research: Oceans*, *125*(11), e2020JC016609. https://doi.org/10.1029/2020JC016609

Karnauskas, K. B., Murtugudde, R., Busalacchi, A. J., Murtugudde, R., & Busalacchi, A. J. (2010). Observing the Galápagos–EUC interaction: Insights and challenges. *Journal of Physical Oceanography*, *40*(12), 2768–2777. https://doi.org/10.1175/2010JPO4461.1

Kawabe, M., & Fujio, S. (2010). Pacific Ocean circulation based on observation. *Journal of Oceanography*, *66*(3), 389–403. https://doi.org/10.1007/s10872-010-0034-8

Kessler, W. S. (2006). The circulation of the eastern tropical Pacific: A review. *Progress in Oceanography*, *69*(2–4), 181–217. https://doi.org/10.1016/j.pocean.2006.03.009

Khon, V. C., Schneider, B., Latif, M., Park, W., & Wengel, C. (2018). Evolution of eastern equatorial Pacific seasonal and interannual variability in response to orbital forcing during the Holocene and Eemian from model simulations. *Geophysical Research Letters*, *45*(18), 9843–9851. https://doi.org/10.1029/2018GL079337

Kienast, S. S., Kienast, M., Jaccard, S., Calvert, S. E., & François, R. (2006). Testing the silica leakage hypothesis with sedimentary opal records from the eastern equatorial Pacific over the last 150 kyrs. *Geophysical Research Letters*, *33*(15). https://doi.org/10.1029/2006GL026651

Kienast, S. S., Kienast, M., Mix, A. C., Calvert, S. E., & François, R. (2007). Thorium-230 normalized particle flux and sediment focusing in the Panama Basin region during the last 30,000 years. *Paleoceanography*, *22*(2). https://doi.org/10.1029/2006PA001357

Klinkhammer, G. P., & Palmer, M. R. (1991). Uranium in the oceans: Where it goes and why. *Earth and Planetary Science Letters*, *55*(7), 1799–1806. https://doi.org/10.1016/0016-7037(91)90024-Y

Koutavas, A., & Joanides, S. (2012). El Niño-southern oscillation extrema in the Holocene and last glacial maximum. *Paleoceanography*, *27*(4), PA4208. https://doi.org/10.1029/2012PA002378

Koutavas, A., Lynch-Stieglitz, J., Marchitto, T. M., & Sachs, J. P. (2002). El Niño-like pattern in ice age tropical Pacific sea surface temperature. *Science*, *297*(5579), 226–230. https://doi.org/10.1126/science.1072376

Lisiecki, L. E., & Raymo, M. E. (2005). A Pliocene-Pleistocene stack of 57 globally distributed benthic $\delta^{18}O$ records. *Paleoceanography*, *20*(1). https://doi.org/10.1029/2004PA001071

Loveley, M., Marcantonio, F., Wisler, M. M., Hertzberg, J. E., Schmidt, M. W., & Lyle, M. (2017). Millennial-scale iron fertilization of the eastern equatorial Pacific over the past 100,000 years. *Nature Geoscience*, *22*(10), 1–764. https://doi.org/10.1038/ngeo3024

Lu, J., Chen, G., & Frierson, D. M. W. (2010). The position of the midlatitude storm track and eddy-driven westerlies in Aquaplanet AGCMs in: Journal of the atmospheric sciences volume 67 issue 12 (2010). *Journal of the Atmospheric Sciences*, *67*, 3984–4000. https://doi.org/10.1175/2010JAS3477.1

Lu, W., Costa, K. M., & Oppo, D. W. (2023). Reconstructing the oxygen depth profile in the Arabian sea during the last glacial period. *Paleoceanography and Paleoclimatology*, *38*(6), e2023PA004632. https://doi.org/10.1029/2023PA004632

Lu, W., Wang, Y., Oppo, D. W., Nielsen, S. G., & Costa, K. M. (2022). Comparing paleo-oxygenation proxies (benthic foraminiferal surface porosity, I/Ca, Authigenic Uranium) on modern sediments and the glacial Arabian Sea. *Geochimica et Cosmochimica Acta*, *331*, 69–85. https://doi.org/10.1016/j.gca.2022.06.001

Madison, A. S., Tebo, B. M., Mucci, A., Sundby, B., & Luther, G. W. (2013). Abundant porewater Mn (III) is a major component of the sedimentary redox system. *Science*, *341*(6148), 875–878. https://doi.org/10.1126/science.1241396

Mangini, A., Jung, M., & Laukenmann, S. (2001). What do we learn from peaks of uranium and of manganese in deep sea sediments? *Marine Geology*, *177*(1–2), 63–78. https://doi.org/10.1016/S0025-3227(01)00124-4

Martínez-García, A., Sigman, D. M., Ren, H., Anderson, R. F., Straub, M., Hodell, D. A., et al. (2014). Iron fertilization of the subantarctic ocean during the last ice age. *Science*, *343*(6177), 1347–1350. https://doi.org/10.1126/science.1246848

Matear, R. J., Hirst, A. C., & McNeil, B. I. (2000). Changes in dissolved oxygen in the Southern Ocean with climate change. *Geochemistry, Geophysics, Geosystems*, *1*(11). https://doi.org/10.1029/2000GC000086

McCorkle, D. C., & Emerson, S. R. (1988). The relationship between pore water carbon isotopic composition and bottom water oxygen concentration. *Geochimica et Cosmochimica Acta*, *52*(5), 1169–1178. https://doi.org/10.1016/0016-7037(88)90270-0

McManus, J., Berelson, W. M., Klinkhammer, G. P., Hammond, D. E., & Holm, C. (2005). Authigenic uranium: Relationship to oxygen penetration depth and organic carbon rain. *Geochimica et Cosmochimica Acta*, *69*(1), 95–108. https://doi.org/10.1016/j.gca.2004.06.023

Menviel, L., & Spence, P. (2024). Southern Ocean circulation's impact on atmospheric CO_2 concentration. *Frontiers in Marine Science*, *10*. https://doi.org/10.3389/fmars.2023.1328534

Mix, A. C., & Tiedmann, B. (2003). Shipboard scientific party, 2003. Site 1240. (No. 202). In *Proceedings of the ocean drilling Program, initial reports*.

Neme, J., England, M. H., & McC. Hogg, A. (2022). Projected changes of surface winds over the Antarctic continental margin. *Geophysical Research Letters*, *49*(16), e2022GL098820. https://doi.org/10.1029/2022GL098820

Orsi, A. H., & Wiederwohl, C. L. (2009). A recount of Ross Sea waters. *Deep Sea Research Part II: Topical Studies in Oceanography, Southern Ocean Shelf Slope Exchange*, *56*(13–14), 778–795. https://doi.org/10.1016/j.dsr2.2008.10.033

Pak, H., & Zaneveld, J. R. V. (1973). The cromwell current on the east side of the Galapagos Islands. *Journal of Geophysical Research*, *78*(33), 7845–7859. https://doi.org/10.1029/jc078i033p07845

Pallone, C. T., McManus, J. F., & Jacobel, A. W. (2025). Eastern equatorial Pacific paleo-productivity and carbon cycling during the late Pleistocene. *Earth and Planetary Science Letters*, *656*, 119255. https://doi.org/10.1016/j.epsl.2025.119255

Pavia, F. J., Wang, S., Middleton, J., Murray, R. W., & Anderson, R. F. (2021). Trace metal evidence for deglacial ventilation of the abyssal Pacific and Southern oceans. *Paleoceanography and Paleoclimatology*, *36*(9), e2021PA004226. https://doi.org/10.1029/2021PA004226

Pena, L. D., Cacho, I., Ferretti, P., & Hall, M. A. (2008). El Niño-Southern Oscillation-like variability during glacial terminations and interlatitudinal teleconnections. *Paleoceanography*, *23*(3). https://doi.org/10.1029/2008PA001620

Perren, B. B., Hodgson, D. A., Roberts, S. J., Sime, L., Van Nieuwenhuyze, W., Verleyen, E., & Vyverman, W. (2020). Southward migration of the Southern Hemisphere westerly winds corresponds with warming climate over centennial timescales. *Communications Earth & Environment*, *1*, 1–8. https://doi.org/10.1038/s43247-020-00059-6

Persch, C. F., DiNezio, P., & Lovenduski, N. S. (2023). The impact of orbital precession on air-sea CO_2 exchange in the Southern Ocean. *Geophysical Research Letters*, *50*(21), e2023GL103820. https://doi.org/10.1029/2023GL103820

Pichevin, L. E., Reynolds, B. C., Ganeshram, R. S., Cacho, I., Pena, L., Keefe, K., & Ellam, R. M. (2009). Enhanced carbon pump inferred from relaxation of nutrient limitation in the glacial ocean. *Nature*, *459*(7250), 1114–1117. https://doi.org/10.1038/nature08101

Rafter, P. A., & Charles, C. D. (2012). Pleistocene equatorial Pacific dynamics inferred from the zonal asymmetry in sedimentary nitrogen isotopes. *Paleoceanography*, *27*(3). https://doi.org/10.1029/2012PA002367

Rafter, P. A., Sigman, D. M., & Mackey, K. R. M. (2017). Recycled iron fuels new production in the eastern equatorial Pacific Ocean. *Nature Communications*, *8*(1), 1100. https://doi.org/10.1038/s41467-017-01219-7

Reimi, M. A., Marcantonio, F., Stieglitz, J. L., Jacobel, A. W., McManus, J. F., & Winckler, G. (2019). The penultimate glacial termination and variability of the Pacific intertropical convergence zone. *Geophysical Research Letters*, *46*(9), 4826–4835. https://doi.org/10.1029/2018GL081403

Reitz, A., Pfeifer, K., de Lange, G. J., & Klump, J. (2004). Biogenic barium and the detrital Ba/Al ratio: A comparison of their direct and indirect determination. *Marine Geology*, *204*(3–4), 289–300. https://doi.org/10.1016/S0025-3227(04)00004-0

Rickaby, R. E. M., Elderfield, H., Roberts, N., Hillenbrand, C.-D., & Mackensen, A. (2010). Evidence for elevated alkalinity in the glacial Southern Ocean. *Paleoceanography*, *25*(1). https://doi.org/10.1029/2009pa001762

Rippert, N., Max, L., Mackensen, A., Cacho, I., Povea, P., & Tiedemann, R. (2017). Alternating influence of northern versus southern-sourced water masses on the equatorial Pacific subthermocline during the past 240 ka. *Paleoceanography*, *32*(11), 1256–1274. https://doi.org/10.1002/2017PA003133

Robinson, R. S., Martinez, P., Pena, L. D., & Cacho, I. (2009). Nitrogen isotopic evidence for deglacial changes in nutrient supply in the eastern equatorial Pacific. *Paleoceanography*, *24*(4). https://doi.org/10.1029/2008PA001702

Schimmenti, D., Marcantonio, F., Hayes, C. T., Hertzberg, J., Schmidt, M., & Sarao, J. (2022). Insights into the deglacial variability of phytoplankton community structure in the eastern equatorial Pacific Ocean using [^{231}Pa/^{230}Th]xs and opal-carbonate fluxes. *Scientific Reports*, *12*, 1–12. https://doi.org/10.1038/s41598-022-26593-1

Schlitzer, R. (2016). Ocean data View.

Schmidt, C., Morrison, A. K., & England, M. H. (2023). Wind– and sea-ice–driven interannual variability of Antarctic bottom water formation. *Journal of Geophysical Research: Oceans*, *128*(6), e2023JC019774. https://doi.org/10.1029/2023JC019774

Shackleton, N. J., Hall, M. A., Line, J., & Shuxi, C. (1983). Carbon isotope data in core V19-30 confirm reduced carbon dioxide concentration in the ice age atmosphere. *Nature*, *306*(5941), 319–322. https://doi.org/10.1038/306319a0

Sigman, D. M., & Boyle, E. A. (2000). Glacial/interglacial variations in atmospheric carbon dioxide. *Nature*, *407*(6806), 859–869. https://doi.org/10.1038/35038000

Sigman, D. M., & Hain, M. P. (2024). Ocean oxygen, preformed nutrients, and the cause of the lower carbon dioxide concentration in the atmosphere of the last glacial maximum. *Paleoceanography and Paleoclimatology*, *39*(1), e2023PA004775. https://doi.org/10.1029/2023PA004775

Sigman, D. M., Hain, M. P., & Haug, G. H. (2010). The polar ocean and glacial cycles in atmospheric CO_2 concentration. *Nature*, *466*(7302), 47–55. https://doi.org/10.1038/nature09149

Sigman, D. M., & Haug, G. H. (2003). 6.18 the biological pump in the past. *Treatise on Geochemistry*, *6*, 491–528. https://doi.org/10.1016/B0-08-043751-6/06118-1

Silvano, A., Foppert, A., Rintoul, S. R., Holland, P. R., Tamura, T., Kimura, N., et al. (2020). Recent recovery of Antarctic bottom water formation in the Ross Sea driven by climate anomalies. *Nature Geoscience*, *13*(12), 780–786. https://doi.org/10.1038/s41561-020-00655-3

Singh, A. K., Marcantonio, F., & Lyle, M. (2011). Sediment focusing in the Panama Basin, Eastern equatorial Pacific Ocean. *Earth and Planetary Science Letters*, *309*(1–2), 33–44. https://doi.org/10.1016/j.epsl.2011.06.020

Singh, A. K., Marcantonio, F., & Lyle, M. (2020). An assessment of xsBa flux as a paleoproductivity indicator and its water-depth dependence in the easternmost equatorial Pacific Ocean. *Paleoceanography and Paleoclimatology*, *35*(12), e2020PA003945. https://doi.org/10.1029/2020PA003945

Skonieczny, C., McGee, D., Winckler, G., Bory, A., Bradtmiller, L. I., Kinsley, C. W., et al. (2019). Monsoon-driven Saharan dust variability over the past 240,000 years. *Science Advances*, *5*(1), eaav1887. https://doi.org/10.1126/sciadv.aav1887

Solodoch, A., Stewart, A. L., Hogg, A. M. C., Morrison, A. K., Kiss, A. E., Thompson, A. F., et al. (2022). How does Antarctic bottom water cross the Southern Ocean? *Geophysical Research Letters*, *49*(7), e2021GL097211. https://doi.org/10.1029/2021GL097211

Spence, P., Griffies, S. M., England, M. H., Hogg, A. M. C., Saenko, O. A., & Jourdain, N. C. (2014). Rapid subsurface warming and circulation changes of Antarctic coastal waters by poleward shifting winds. *Geophysical Research Letters*, *41*(13), 4601–4610. https://doi.org/10.1002/2014GL060613

Stevenson, M., & Taft, B. (1971). New evidence of the equatorial undercurrent east of the Galapagos Islands. *Journal of Marine Research*, *29*.

Stewart, A. L., & Thompson, A. F. (2012). Sensitivity of the ocean's deep overturning circulation to easterly Antarctic winds. *Geophysical Research Letters*, *39*(18). https://doi.org/10.1029/2012GL053099

Stewart, A. L., & Thompson, A. F. (2013). Connecting Antarctic cross-slope exchange with Southern Ocean overturning. *Journal of Physical Oceanography*, *43*(7), 1453–1471. https://doi.org/10.1175/JPO-D-12-0205.1

Suzuki, T., Ishii, M., Aoyama, M., Christian, J. R., Enyo, K., Kwano, T., et al. (2013). PACIFICA data synthesis Project. *ORNL/CDIAC-159*. NDP-092. https://doi.org/10.3334/CDIAC/OTG.PACIFICA_NDP092

Thomas, N. C., Bradbury, H. J., & Hodell, D. A. (2022). Changes in North Atlantic deep-water oxygenation across the middle pleistocene transition. *Science*, *377*(6606), 654–659. https://doi.org/10.1126/science.abj7761

Timmermann, A., Friedrich, T., Timm, O. E., Chikamoto, M. O., Abe-Ouchi, A., & Ganopolski, A. (2014). Modeling obliquity and CO_2 effects on southern hemisphere climate during the past 408 ka. *Journal of Climate*, *27*(5), 1863–1875. https://doi.org/10.1175/JCLI-D-13-00311.1

Timmermann, A., Lorenz, S. J., An, S.-I., Clement, A. C., & Xie, S.-P. (2015). The effect of orbital forcing on the mean climate and variability of the tropical Pacific. *Journal of Climate*, *20*(16), 4147–4159. https://doi.org/10.1175/JCLI4240.1

Toggweiler, J. R., Russell, J. L., & Carson, S. R. (2006). Midlatitude westerlies, atmospheric CO_2, and climate change during the ice ages. *Paleoceanography*, *21*(2), PA2005. https://doi.org/10.1029/2005PA001154

Weber, M. E., Wiedicke, M., Riech, V., & Erlenkeuser, H. (1995). Carbonate preservation history in the Peru Basin: Paleoceanographic implications. *Paleoceanography*, *10*(4), 775–800. https://doi.org/10.1029/95PA01566

Winckler, G., Anderson, R. F., Jaccard, S. L., & Marcantonio, F. (2016). Ocean dynamics, not dust, have controlled equatorial Pacific productivity over the past 500,000 years. *Proceedings of the National Academy of Sciences*, *113*(22), 6119–6124. https://doi.org/10.1073/pnas.1600616113

Zhang, P., Xu, J., Holbourn, A., Kuhnt, W., Beil, S., Li, T., et al. (2020). Indo-pacific hydroclimate in response to changes of the intertropical convergence zone: Discrepancy on precession and obliquity bands over the last 410 kyr. *Journal of Geophysical Research: Atmospheres*, *125*(14), e2019JD032125. https://doi.org/10.1029/2019JD032125

Zhang, S., Yu, Z., Gong, X., Wang, Y., Chang, F., Lohmman, G., et al. (2021). Precession cycles of the El Niño/Southern oscillation-like system controlled by Pacific upper-ocean stratification. *Communications Earth & Environment*, *2*, 1–10. https://doi.org/10.1038/s43247-021-00305-5